International Journal of Nanomedicine

Dovepress
Taylor & Francis Group

Open Access Full Text Article

ORIGINAL RESEARCH

Safety, Efficacy and Bio-Distribution Analysis of Exosomes Derived From Human Umbilical Cord Mesenchymal Stem Cells for Effective Treatment of Bronchopulmonary Dysplasia by Intranasal Administration in Mice Model

Wanting Xu[1–3], Xiaolin Jieda[1–3], Yue Wu[1–3], Fengling Du[1–3], Lu Ma[1–3], Lijuan Luo[1–3], Dong Liu[1–3], Ling Guo[3], Jing Liu[3], Wenbin Dong[1–3]

[1]Division of Neonatology, Department of Pediatrics, the Affiliated Hospital of Southwest Medical University, Luzhou, 646000, People's Republic of China; [2]Department of Perinatology, The Affiliated Hospital of Southwest Medical University, Luzhou, 646000, People's Republic of China; [3]Sichuan Clinical Research Center for Birth Defects, The Affiliated Hospital of Southwest Medical University, Luzhou, 646000, People's Republic of China

Correspondence: Wenbin Dong, Division of neonatology, Department of Pediatrics, the Affiliated Hospital of Southwest Medical University; Department of Perinatology, The Affiliated Hospital of Southwest Medical University; Sichuan Clinical Research Center for Birth Defects, Luzhou, 646000, People's Republic of China, Email dongwenbin2000@163.com

Purpose: Exosomes (Exos) derived from human umbilical cord mesenchymal stem cells (hUC-MSCs) hold great potential for treating bronchopulmonary dysplasia (BPD); however, safety concerns and effects of intranasal administration remain unexplored. This study aimed to explore the safety of hUC-MSCs and Exos and to investigate the efficacy and bio-distribution of repeated intranasal Exos administration in neonatal BPD models.

Methods: Characteristics of hUC-MSCs and Exos were analyzed. A subcutaneous tumor formation assay using a single dose of hUC-MSCs or Exos was conducted in Crl:NU-Foxn1nu mice. Vital signs, biochemical indices, pathological alterations, and ^{18}F-FDG microPET/CT analysis were examined. Pulmonary pathology, three-dimensional reconstructions, ultrastructural structures, in vivo and ex vivo bio-distribution imaging analyses, enzyme-linked immunoassay assays, and reverse transcription-quantitative polymerase chain reaction analyses of lung tissues were all documented following intranasal Exos administration.

Results: Characteristics of hUC-MSCs and Exos satisfied specifications. Crl:NU-Foxn1nu mice did not exhibit overt toxicity or carcinogenicity following a single dose of hUC-MSCs or Exos after 60 days of observation. Repeated intranasal Exos administration effectively alleviated pathological injuries, restored pulmonary ventilation in three-dimensional reconstruction, and recovered endothelial cell layer integrity in ultrastructural analysis. Exos steadily accumulated in lung tissues from postnatal day 1 to 14. Exos also interrupted the epithelial–mesenchymal transition and inflammation reactions in BPD models.

Conclusion: As a nanoscale, non-cellular therapy, intranasal administration of Exos was an effective, noninvasive treatment for BPD. This approach was free from toxic, tumorigenic risks and repaired alveolar damage while interrupting epithelial–mesenchymal transition and inflammation in neonatal mice with BPD.

Plain language summary: This study aimed to address the safety concerns surrounding hUC-MSCs and Exos and to investigate, for the first time, the bio-distribution and efficacy of repeated intranasal administration of Exos in a neonatal BPD model. Repeated intranasal Exos administration significantly ameliorated pulmonary pathological injuries and predominantly accumulated in the lungs, as demonstrated by fluorescence tracking from the first day after birth. Furthermore, Exos reduced epithelial–mesenchymal transition and inflammatory cytokines in BPD models. These findings suggest that intranasal administration of Exos is a safe, effective, and noninvasive approach to treat BPD without toxic or tumorigenic risks. Intranasal exos as a nanoscalic, non-cellular therapy has a significant potential for the treatment of BPD, although further examinations are necessary to fully clarify their mechanisms and long-term effects.

Received: 20 October 2024
Accepted: 4 February 2025
Published: 27 February 2025

Keywords: BPD, Exos, intranasal administration, safety, efficacy, bio-distribution analysis

Introduction

Bronchopulmonary dysplasia (BPD) is the most common and severe chronic respiratory disease in premature infants. It is characterized by alveolar simplification, impaired secondary alveolar septation, and disrupted pulmonary microvascular development, typically occurring during the saccular phase or earlier and often accompanied by fibrosis.[1–3] With advancements in perinatal medical care, including the use of postnatal corticosteroids in at-risk preterm infants, less invasive surfactant administration, and non-invasive ventilatory support in the delivery room, have significantly reduced the risk of death and disability in preterm infants.[4–7] Despite these advances, the incidence of BPD has remained unchanged.[8] Recent studies indicate that incidences of BPD in preterm infants range from 2.4% to 71.6%, varying with gestational age (GA) and birth weight.[9,10] BPD is a multifactorial disorder related to several long-term sequelae, including impaired respiratory function, neurodevelopmental delays, and motor dysfunction.[11] Its effects can persist into adolescence, profoundly impacting quality of life and placing a substantial burden on families. As a result, there is an urgent need to identify effective and safe treatment options for BPD. Oxygen supplementation is essential for premature infants; however, prolonged exposure to hyperoxia is a major contributing factor to BPD development.[12]

Graphical Abstract

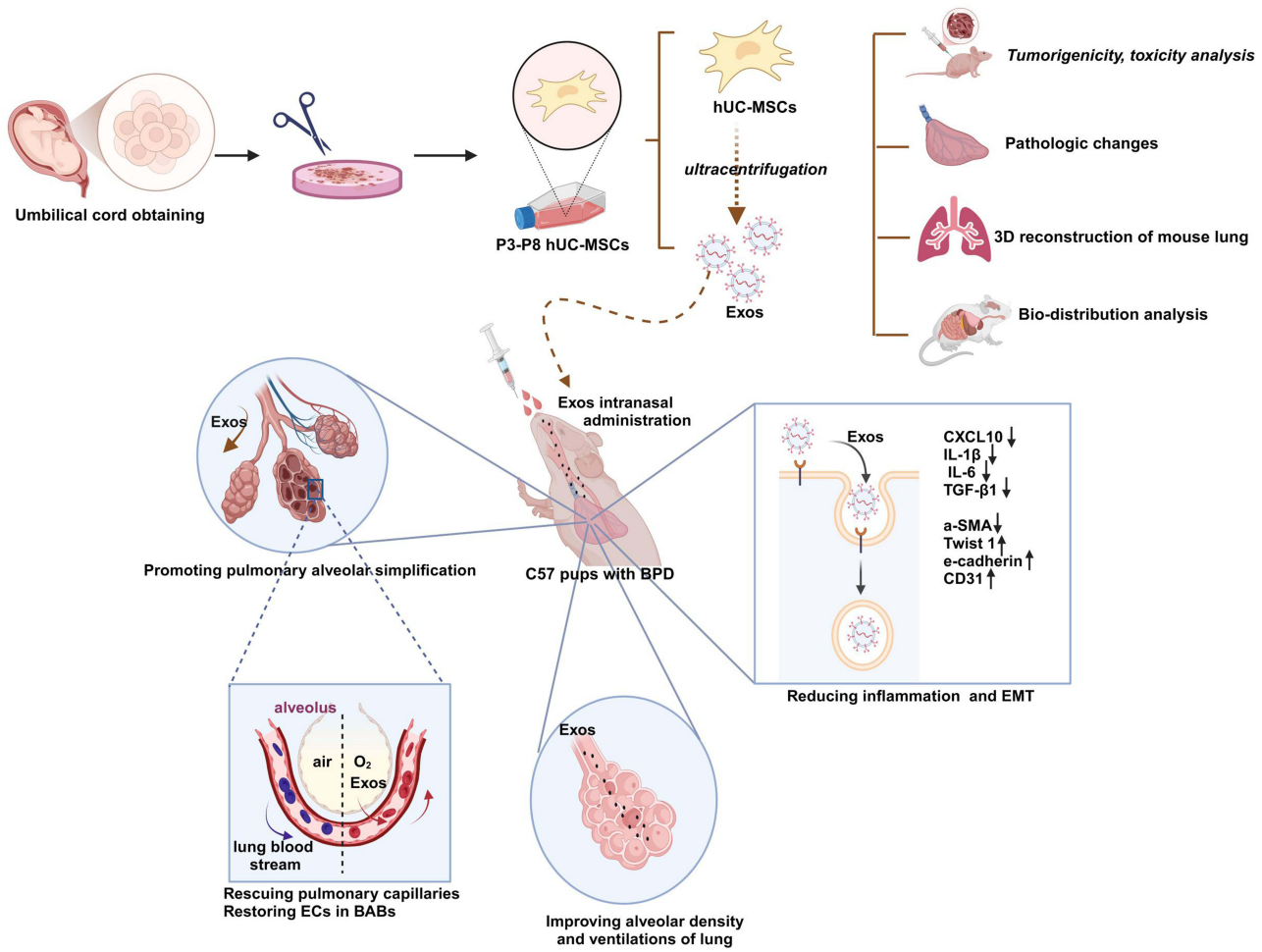

Due to the immaturity of the body's antioxidant system, exposure to high oxygen concentrations can induce excessive oxidative stress, resulting in alveolar epithelial cell damage, impaired gas exchange, and pulmonary fibrosis (PF). These effects are mediated by the promotion of epithelial–mesenchymal transition (EMT) and the upregulation of inflammatory cytokines.[13–15] A well-established model for replicating the BPD phenotype involves hyperoxic exposure in newborn mice. This model demonstrates key features of BPD, including pulmonary edema, alveolar simplification, disordered angiogenesis, fibrin deposition, and inflammatory injury, closely resembling the pulmonary pathology observed in humans.[16–18]

The hUC-MSCs have emerged as a promising candidate for BPD treatment due to their ability to mitigate oxidative stress, suppress inflammatory cytokine production, and promote alveolarization and angiogenesis in neonatal rats exposed to hyperoxia conditions.[19,20] A recent Phase I clinical trial with a two-year follow-up demonstrated that repeated intravenous doses of hUC-MSCs in extremely low-gestational age neonates (ELGANs) at high risk of BPD were not linked to morality or serious adverse events.[21] Despite significant progress, challenges are persistent in the direct application of hUC-MSC therapy. These challenges include ethical concerns related to sources of hUC-MSCs, the standardization of hUC-MSC culture and therapeutic efficacy, microvascular occlusion, tumorigenic risks, and pathogen transmission.[22,23]

Extracellular vesicles (EVs) obtained from hUC-MSCs have drawn attention as a potentially safer and more targeted substitute due to these challenges. EVs are generally classified into three main subtypes: exosomes, microvesicles, and apoptotic bodies, based on size, segmentation parameters, contents, and transmembrane proteins. Exos are nanosized particles secreted by all cell types that play a role in intercellular communication by transporting proteins, lipids, and RNA to sites of neonatal lung disease, and are considered as a new way of cell-to-cell communication.[24,25] Unlike hUC-MSCs, Exos do not carry the same risk of transplant-related side effects, making them an attractive option for clinical use. Exos derived from hUC-MSCs retain similar biological functions, including anti-inflammatory and regenerative capabilities, while raising less safety concerns.[26,27] Studies have demonstrated that Exos alleviate inflammation and oxidative stress damage, promote angiogenesis, and enhance alveolarization, indicating their potential to address key pathological aspects of BPD.[28–30] Exos obtained from hUC-MSCs present a promising avenue for treating BPD, offering regenerative and immunomodulatory benefits while mitigating the risks associated with direct hUC-MSC transplantation.[31,32] The hUC-MSCs are considered an ideal source for producing Exos due to their non-invasive isolation, rapid self-renewal, proliferation capabilities, and comparable immunomodulatory properties, facilitating lung tissue repair.[31,33] However, a prior study highlighted the potential toxicity of various nanoparticles in vivo and ex vivo, warranting further investigation.[34]

Although Exos are a type of nanoparticles, there is currently no international standard for determining the safe dosage in mice or for assessing their biodistribution following intranasal administration in the BPD model.[35] GW4869 inhibits the neutral sphingomyelin 2 (NSMase2) and thereby blocks the synthesis and secretion of Exos, which could serve as an Exos inhibitor in vivo and ex vivo.[36] To address this knowledge gap, this research used a newborn hyperoxia-exposed C57BL/6J mouse model of BPD to investigate the therapeutic effects of Exos in vivo. Given the significant potential of Exos in rescuing BPD, this research primarily focused on culturing hUC-MSCs and administering Exos noninvasively via continuous nasal drip.

Materials and Methods

This research adhered to the principles outlined in the Declaration of Helsinki and received approval from the Ethics Committee of Southwest Medical University (License Number: KY 2023269). Written informed consent was obtained from all umbilical cord donors. All animal procedures were conducted in compliance with the Animal Ethics Procedures and Regulations of the People's Republic of China. All animal experiments were approved by the Southwest Medical University Animal Ethical and Experimental Committee (License Number: 20241024–016). Pregnant wild-type C57BL/6J mice (6–8 weeks old) were obtained from the Experimental Center of Southwest Medical University (Sichuan, China), while male athymic nude mice (Crl:NU-Foxn1nu) were purchased from Vital River Laboratory Animal Technology Co., Ltd. (Sichuan, China). All mice were housed in a specific pathogen-free facility within the experimental animal center, with fully automated temperature control (22°C ± 2°C) and humidity (50% ± 5%). Animals were maintained on a 12:12-

hour light–dark cycle with free access to food and water. All surgical procedures were conducted under isoflurane anesthesia to minimize animal suffering.

Cell Culture and Characterizations

The hUC-MSCs were isolated from the umbilical cord tissue of healthy full-term infants at the time of delivery at the Affiliated Hospital of Southwest Medical University. Fresh umbilical cord tissue was thoroughly washed with phosphate-buffered saline (PBS, C0221A, Beyotime, China), minced using sterile surgical scissors, digested with 0.25% collagenase type II (C8150, Solarbio, China) for 50 min at 37°C, and centrifuged at 1000 g for 15 min. The resulting cell pellet was resuspended in a culture medium consisting of Dulbecco's Modified Eagle Medium (DMEM/F12, 12634010, Thermo Fisher, USA) supplemented with 20% fetal bovine serum (FBS, ST30-3031, Pan Seratech, Germany) and maintained at 37°C with 5% CO_2. The culture medium was changed for the first time on the fifth day and subsequently replaced every three days. hUC-MSCs were maintained at passage 3 (P3) in a serum-free maintenance medium (CF0101, Crgen, China) and stored in the gas phase of liquid nitrogen for long-term preservation. Routine subculturing was performed using 0.25% trypsin without EDTA (C0205, Beyotime, China) once the cells reached over 85% confluence. Specific staining was conducted using Alizarin Red S (PD-017, Procell, China), Alcian Blue (PD-018, Procell, China), and Oil Red O (PD-019, Procell, China) to confirm the differentiation into osteocytes, chondrocytes, and adipocytes, respectively, following the manufacturers' protocols. Morphological analysis and flow cytometry assays were employed to identify hUC-MSCs.

Soft-Agar Colony Formation Assay

The tumorigenicity of hUC-MSCs was assessed using a soft agar colony formation assay ex vivo. The hUC-MSCs (1×10^3 cells per well) of P3 were seeded into a biofree 6-well plate, containing a 0.7% low-melting point agarose layer, with a 1.2% agarose overlay (A8350, Solarbio, China). The highly aggressive human melanoma cell line A375 was used as a positive control. The less aggressive human lung epithelial cell line Beas-2B served as the negative control. Complete culture medium was used as the blank control. The cells were incubated at 37°C with 5% CO_2 for 28 days, with medium changes every three days. Colonies were observed under inverted phase contrast microscopy (Olympus, Tokyo, Japan).

Isolations and Characterizations of Exos and DiR-Exos

P3 to P8 hUC-MSCs were cultured, and their culture supernatants were concentrated using a 100-kDa molecular weight cutoff membrane (UFC9100, Millipore, USA). The supernatants were sequentially centrifuged at 500 × g for 10 min, 3000 × g for 15 min, and 11,000 × g for 30 min to remove dead cells. Subsequently, the supernatants were ultracentrifuged at 4°C and 100,000 × g for 70 min. The resulting pellets were resuspended in PBS, followed by a second ultracentrifugation under the same conditions. The final pellets of Exos were resuspended in sterile PBS and stored at −80°C for subsequent experiments. Additionally, DiR was combined with Exos at ratio of 2 μg DiR/100 μg Exos in sterile PBS solution for 30 min at 37°C in the absence of light, followed by ultracentrifugation at 100,000 × g for 70 min. Transmission electron microscopy (TEM) was used to examine morphological properties. Exos or DiR-Exos were dropped onto a copper grid with 10 μL and stained with 2% uranyl acetate solution for 1 min and air-dried. Their images were captured using TEM at a magnification of 20,000 ×. Nanoparticle tracking analysis (NTA; Malvern, China) was used to analyze the particle size of Exos and DiR-Exos, and zeta potential measurements were used to determine the surface charge. The extracted particles were diluted to a concentration between 1×10^7 and 1×10^9 particles/mL with pure water. After removing the air bubbles from the sample chamber, the particle sizes and surface charge were analyzed. The identity of the isolated Exos was confirmed by Western blot analysis for the surface markers CD9 (60232, Proteintech, China), CD63 (67605, Proteintech, China), CD81 (27855, Proteintech, China), TSG101 (67381, Proteintech, China), and Calnexin (66903, Proteintech, China). The protein ladders used for Western blotting were PageRuler™ Prestained Protein Ladders (26616, Thermo Fisher, USA).

The Animal Studies Using Athymic Nude Mice

A total of 32 male Crl:NU-Foxn1nu mice, aged 4–5 weeks, weighing 20–21g, were randomly divided into four groups: the control group, the A375 group, the hUC-MSC group, and the Exos group, with eight mice per group. All mice were housed in a specific pathogen-free (SPF) environment. To establish a transplantation model, 0.2 mL of P3 hUC-MSCs 5 $\times 10^6$ cells/kg cell suspension was subcutaneously injected into the right back of the mice into the nude mice. The control group received 0.2 mL cell diluent PBS solution and the A375 group received 0.2 mL A375 5 $\times 10^6$ cells/kg cell suspension injected subcutaneously. Each nude mouse in the Exos group was injected with 0.2 mL 1 $\times 10^7$ particles/g Exos subcutaneously. The subcutaneous injection dose of hUC-MSCs was based on a previous study using nude mice.[37] The dose of Exos was referred to the formula from *Experimental Zoology*, with the dose for nude mice to 1.4 $\times 10^7$ particles/g according to body surface area. Tumor diameter, length, body weight, and food consumption for each mouse were recorded every other day, beginning one week after injection. Tumor volume was calculated twice weekly using the formula: volume = length $\times$ width^2 $\times$ 0.5.

The Critical Micro PET-CT Scan Analysis

Three Crl:NU-Foxn1nu mice per group were scanned using MicroPET/CT (Siemens, Munich, Germany) on day 30 post-injection. The radiochemical purity of ^{18}F-FDG exceeded 95%. Before the experiment, the mice were fasted for 12 hours. A bolus injection of 3.7 MBq (100 μL) of ^{18}F-FDG was administered intravenously via the tail vein, followed by a 60-min imaging acquisition period. Anesthesia was induced with a 2% isoflurane-oxygen mixture administered 20 min before scanning. The mice were positioned prone on the PET/CT imaging bed. The following scanning parameters were applied for a 10-min scan: 500 μA, 80 kV, and 1.8 mm disk collimation. A volume of interest (VOI) was manually delineated on the CT images, and the coregistered PET/CT images were used for further analysis. Semi-quantitative assessment of ^{18}F-FDG uptake in the tumor tissue was conducted, with the maximum (SUV $_{max}$) and mean (SUV $_{mean}$) standard uptake values calculated based on the peak and average radioactivity concentrations within the VOI. The InliView-01B software performed a semi-quantitative analysis to define the metabolic volume (MV) within the contours, using a 40% threshold of SUV_{max}.

Plasma Index Measurement and Pathological Changes

The observation period for tumor-bearing Crl:NU-Foxn1nu mice was extended to 60 days. The experiments were terminated for ethical considerations when the weight loss in the nude mice exceeded 20% or clinical symptoms were severe. Blood samples were collected on the day 31st and 60th post-injection, prior to euthanasia, and centrifuged at 2000 rpm for 5 min at 4°C. The serum was then subjected to biochemical testing to assess toxicity, including glucose (GLU) and liver function markers such as lactate dehydrogenase (LDH), alkaline phosphatase (ALP), aspartate aminotransferase (AST), and alanine aminotransferase (ALT). Kidney function indicators, including blood urea nitrogen (BUN), creatinine (CREA), and uric acid (UA), were also measured. Organ coefficients, considered a key index of chronic toxicity, were calculated as percentages representing the proportion of body weight attributed to each organ. Additionally, primary organs and tumors were individually extracted, weighed, recorded, and photographed on days 31 and 60 post-injection. These samples were fixed in 4% paraformaldehyde (PFA, P0099, Beyotime, China), embedded in paraffin, and sectioned into 5-μm slices for hematoxylin and eosin (H&E, AWI0443a, Abiowell, China) staining.

Telomerase Activity Detection

Reverse transcription-quantitative polymerase chain reaction (RT-qPCR) was employed to evaluate the telomerase activity of A375 cells, hUC-MSCs, and Exos. Total RNA from A375 cells and hUC-MSCs was extracted using a total RNA isolation kit (RC112, Vazyme, China) according to the manufacturer's protocol. For Exos, total RNA was isolated using TRIzol reagent (R411, Vazyme, China). RNA samples (1000 ng each) were reverse transcribed into complementary DNA (cDNA) using HiScript III RT SuperMix for qPCR (R323, Vazyme, China) according to the manufacturer's instructions. Real-time quantitative PCR was performed using ChamQ Universal SYBR qPCR Master Mix (Q711, Vazyme, China) on a QuantStudio 3 Real-Time PCR System (A28567, Thermo Fisher, USA), with GAPDH as the

internal control. The thermal cycling conditions were 15 min at 37 °C, 5 sec at 85 °C, followed by 5 min at 95 °C, and 40 cycles of 10 sec at 95 °C and 30 sec at 60 °C. The relative quantification of telomerase reverse transcriptase (TERT, QH05865S, Biotime, China) mRNA expression was calculated using the cycle threshold ($2^{\wedge-\Delta\Delta Ct}$) method.

Treatment of Newborn Mice

Within 12 hours of birth, newborn C57BL/6J mice were randomly assigned to either the normoxia or hyperoxia group. The hyperoxia group was placed in a sealed hyperoxic chamber with a constant oxygen flow rate of 2 L/min, maintaining an oxygen concentration of 85%. The normoxia group was kept in the same room and exposed to normal oxygen concentration (21%). To minimize excessive oxygen toxicity, the dams were rotated between the normoxia and hyperoxia groups every 24 hours. The hyperoxia chamber was cleaned for 30 min daily after being opened. Four experimental groups of neonatal mice were established: normoxia, hyperoxia, hyperoxia+exosomes, and hyperoxia+GW4869. In the hyperoxia+exosomes group, mice received 2×10^6 particles/g of Exos via nasal injection into both nostrils every other day from postnatal day (PND) 1 to PND 14, totaling seven doses. Similarly, mice in the hyperoxia+GW4869 group received 2 μg of GW4869 nasally every other day from PND 1 to PND 14, for a total of seven doses (14 μg per mouse), also administered into both nostrils using a micropipette. Body weight, growth condition, response, and survival rate were recorded daily. Ten neonatal mice were randomly selected and euthanized under isoflurane anesthesia at the end of PND 1, 3, 5, 7, and 14, under hyperoxic exposure. The left lung was preserved in 4% paraformaldehyde for histopathological analysis, while the right lung was stored at −80°C for RT-qPCR and enzyme-linked immunosorbent assay (ELISA) analysis.

Hematoxylin-Eosin Staining

After fixing the lung tissue in 4% paraformaldehyde for 24 hours, it was paraffin-embedded, baked, deparaffinized, and rehydrated with xylene. The tissue sections, cut at 5 μm, were stained with H&E. Using a digital section scanner (KF-PRO-002, Biolink, China), 10 random areas of each section were captured at 20× magnification. A semi-quantitative analysis was performed, with two pathology professors evaluating the extent of lung damage. Pathological alterations included inflammatory cell infiltration, lung tissue congestion, bleeding, pulmonary edema, alveolar wall thickening, and hyaline membrane formation.[38] The lung injury scores ranged from 0 to 8, with 0 indicating no injury (normal), 2 indicating mild injury (less than 25% of the visual field affected), 4 indicating moderate injury (up to 50% of the visual field affected), 6 indicating severe injury (up to 75% of the visual field affected), and 8 indicating extremely severe injury (widespread damage to the visual field). The inflammation grade of the alveolar interstitium was determined based on the extent of inflammatory cell infiltration, scored on a scale from 0 to 3.[39] A score of 0 indicated no or occasional inflammatory cells, 1 indicated a few loosely arranged inflammatory cells, 2 indicated numerous cells in interstitial and intra-alveolar spaces, and 3 indicated abundant inflammatory cells in the perivascular space. The radical alveolar count (RAC) was determined by counting the number of alveoli intersected by a vertical line drawn from the edge of the terminal bronchus to the nearest pleural or mediastinal border. Alveolar wall thickness was measured using Image J software, by drawing a line across the center of the alveolar wall, measuring its length, and counting the number of alveoli intersected by the line. The mean linear intercept (MLI) was calculated, excluding large tracheids and vessels. In 10 parenchymal areas of the same sample, secondary septal counts were manually recorded by dividing the number of septal tips by the total number of alveolar spaces per field.

Microcomputed Tomography Acquisition

Five mouse pups per group were monitored for two weeks, with microcomputed tomography (*μ-CT*) images captured on the PND 1, 3, 5, 7, and 14. Neonatal C57BL/6J mice were used for the evaluations, which were conducted using a Siemens Inveon CT scanner (Erlangen, Germany). To minimize the inter-mouse variability, dynamic *μ-CT* imaging was employed to assess lung structural changes in the same individual mice over time. This longitudinal approach offers significant advantages for evaluating multiple cohorts at specific time points, including the ability to quantify individual mice over time and perform pairwise statistical evaluations of lung parameters. It also reduces the number of animals required for each experiment, providing ethical and financial benefits. Mice were anesthetized with 2% isoflurane in 90%

oxygen and positioned prone for imaging. Prior to each scan, system calibration was performed using a standard phantom to evaluate noise levels, contrast, uniformity, and resolution. The X-ray voltage was set to 80.0 kV, with a tube current of 0.5 mA, and the X-ray spectrum was filtered with a 0.18 mm filter placed in front of the mouse. Lung samples were scanned over a 360° rotation for 1 min and 30 sec to capture overall lung parameters. Lung volume was quantified in Hounsfield units (HUs) using three-dimensional (3D) Slicer™ software. Mean lung density was measured semi-quantitatively using 3D reconstruction models of lung tissue, excluding major blood vessels, the trachea, and the heart, and focusing on regions of interest. This study introduces a novel algorithm, informed by recent research, to more accurately segment lung tissue regions based on HUs thresholds: −860 to −435 hU for normally aerated regions, −434 to −121 hU for poorly aerated regions, and −120 to 120 hU for non-aerated regions.[40,41] Additionally, volume calculations for various pulmonary ventilation states and the percentage of pulmonary CT-aerated volume were recorded.

Bio-Distribution of Exos

A solution of 1.1'-dioctadecyl-tetramethylindotricarbocyanine iodide (DiR) (D12731, Thermo Fisher, USA) was dissolved in dimethyl sulfoxide (DMSO) (D8371, Solarbio, China) at a concentration of 1 mg/mL to label Exos in vivo. DiR was combined with Exos at a ratio of 2 μg DiR to 100 μg Exos in sterile PBS solution, incubated for 30 minutes at 37°C in the absence of light, and ultracentrifuged at 100,000 g for 70 min. The resulting pellet was resuspended in PBS to a final concentration of 2 μg/μL. Neonatal mice were intranasally administered PBS, Exos, or DiR-labeled Exos (DiR-Exos) under hyperoxic conditions. Each mouse received a total of 1.4×10^7 particles/g of Exos intranasally, with 2×10^6 particles/g administered every other day for seven consecutive doses. Following intranasal administration, the mice were euthanized, and fluorescence imaging was performed on the whole body and vital organs using an IVIS Lumina imaging system (FXPRO, Thermo Fisher, USA). The average radiant efficiency was analyzed using the Living Image 4.7.2 software (excitation = 750 nm, emission = 780 nm).

The Electron Microscopy

Left lung tissue from newborn mice exposed to hyperoxia was processed for TEM as follows: 1 mm^3 of lung tissue was fixed in a modified Karnovsky fixative containing 2.5% glutaraldehyde. The tissue was washed with 100 mm sodium cacodylate buffer, followed by fixation in 1.25% potassium ferricyanide and 1% osmium tetroxide for 2 hours. The tissue was then washed three times with sterile water, dehydrated using graded acetonitrile, and embedded in epoxy resin overnight. Specimens were then divided into 60 nm ultrathin chapters, double-stained with aluminum citrate and uranyl acetate, and examined with a TEM (JEM-1400Flash, JEOL Co., Ltd., Japan). Images were captured using a Hamamatsu side-mounted digital camera (MA01801, Woburn, USA).

Enzyme-Linked Immunosorbent Assay

Frozen lung tissues from neonatal mice were homogenized using a homogenizer with the addition of lysis buffer and centrifuged at 10,000 g for 15 min. The supernatants were collected for analysis. According to the manufacturer's instructions, the levels of C-X-C motif chemokine 10 (CXCL10, SYP-M0014QX, Upingbio, China), interleukin-1 beta (IL-1β, SYP-M0026, Upingbio, China), interleukin-6 (IL-6, SYP-M0031, Upingbio, China), and transforming growth factor beta 1 (TGF-β1, SYP-M0416, Upingbio, China) in the lung tissues were measured using ELISA kits. Absorbance at 450 nm was detected with an Epoch microplate reader (A51119700C, Thermo Fisher, USA).

Immunohistochemistry

Immunohistochemistry (IHC) analysis was performed to assess the expression of several relevant proteins. Lung tissue sections (5 μm thick) from PND 14, embedded in paraffin, were prepared in advance. These samples underwent sequential treatments, including deparaffinization, permeabilization, and hydration, by immersion in a 0.2% Triton X-100 solution in 1× PBS for 15 min at room temperature. Blocking was performed using 10% goat serum for the next step. The tissue sections from the four groups were incubated overnight at 4 °C with primary antibodies against α-SMA (1:5000, ET1607-53), CD31 (1:200, ER31219), E-cadherin (1:500, EM0502), and Twist1 (1:200, EM1710-24), all obtained from Huaan Biotechnology Co., Ltd. (Hangzhou, China). After washing with PBS, the sections were incubated

with HRP-conjugated goat anti-rabbit IgG (1:100, HA1001) or goat anti-mouse IgG (1:100, HA1006) for 1 hour. Following additional washes, staining was performed using 3.3'-Diaminobenzidine (DAB) solution, followed by hematoxylin counterstaining. The slides were dehydrated and sealed. Five nonoverlapping regions were independently selected by two pathologists from each group, resulting in a total of ten regions per group. Average optical density (AOD) and positively stained brownish-yellow particles were analyzed using Image J software. Pulmonary vascular density was calculated using the following formula: pulmonary vascular density (%) = (regions positively stained by lung tissue endothelial cells (EC) for CD31)/(the total area of lung parenchyma) × 100%.

Genotypic Assessment

On day 14, the mRNA expressions of Twist1, E-cadherin, CD31, α-SMA, IL-1β, IL-6, TGF-β, and CXCL10 were measured using RT-qPCR. Total RNA from each group was extracted using a total RNA isolation kit (RC112, Vazyme, China) according to the manufacturer's instructions. The concentration and quality of RNA were assessed using the Nanodrop One Spectrophotometer (Thermo Fisher, USA). Reverse transcription was performed to synthesize complementary DNA (cDNA) (R323, Vazyme, China) from 1000 ng of RNA from each group. The specific primer sequences used for PCR reactions are provided in Supplementary 1.

Statistical Analysis

Statistical analyses were performed using GraphPad Prism version 9.5.1 (GraphPad Software, La Jolla, USA; www.graphpad.com). Data are presented as mean ± standard deviation (SD). A two-independent-sample *t*-test was used for comparisons between two groups, while a one-way analysis of variance (ANOVA) was used for comparisons among more than two groups. A *P*-value of <0.05 was considered statistically significant.

Results

Isolation and Characteristics of hUC-MSCs

After seven days of planting, inverted phase contrast microscopy revealed migrated hUC-MSCs. The cells showed a tendency to stabilize and homogenize before being subcultured to the third passage. Passage 3 (P3) hUC-MSCs were densely packed and displayed a paralleled or whirlpooled pattern, resembling normal spindle firbroblast-like cells (Figure 1A). Following three weeks of osteogenic induction, the hUC-MSCs exhibited positive Alizarin Red S staining (Figure 1B), while positive Alicante Blue staining indicated strong chondrogenic differentiation (Figure 1C). Identification of hUC-MSCs was further confirmed by Oil Red O staining after two weeks of ex vivo adipogenic differentiation (Figure 1D). Flow cytometry analysis showed that the immunophenotype of hUC-MSCs was positive for cell-specific biomarkers such as CD73, CD44, CD29, and CD166, negative for CD11b, CD34, CD45, and IgG1kappa (Figure 1E). In summary, these findings confirm that the hUC-MSCs were successfully isolated and characterized, making them suitable for further research.

Colony Formation Assay ex vivo

The tumorigenicity of hUC-MSCs exposed to prolonged hyperoxia was assessed by soft-agarose colony formation. As expected, a number of A375 cell colonies were observed as a positive control (Figure 1F), whereas Beas-2b (Figure 1G), hUC-MSCs (Figure 1H), and the blank control (Figure 1I) showed no signs of colony formation after four weeks of soft agarose culture. Compared to hUC-MSCs and Beas-2b cells, which did not exhibit any discernible colony formation, A375 cells produced a significantly higher number of colonies in soft agar. Clone numbers of hUC-MSCs and Beas-2b cells showed no statistically significant difference (Figure 1J). These findings collectively demonstrate that prolonged exposure to hyperoxic conditions successfully preserved the non-oncogenicity property of hUC-MSCs ex vivo.

Characterization of Exos and DiR-Exos

TEM analysis revealed that Exos exhibited biconcave structures, restricted to lipid bilayers (Figure 2A). Exos and DiR-Exos were characterized by nanoparticle tracking analysis (NTA), with median diameter ranging from 120.9 nm to 133.7

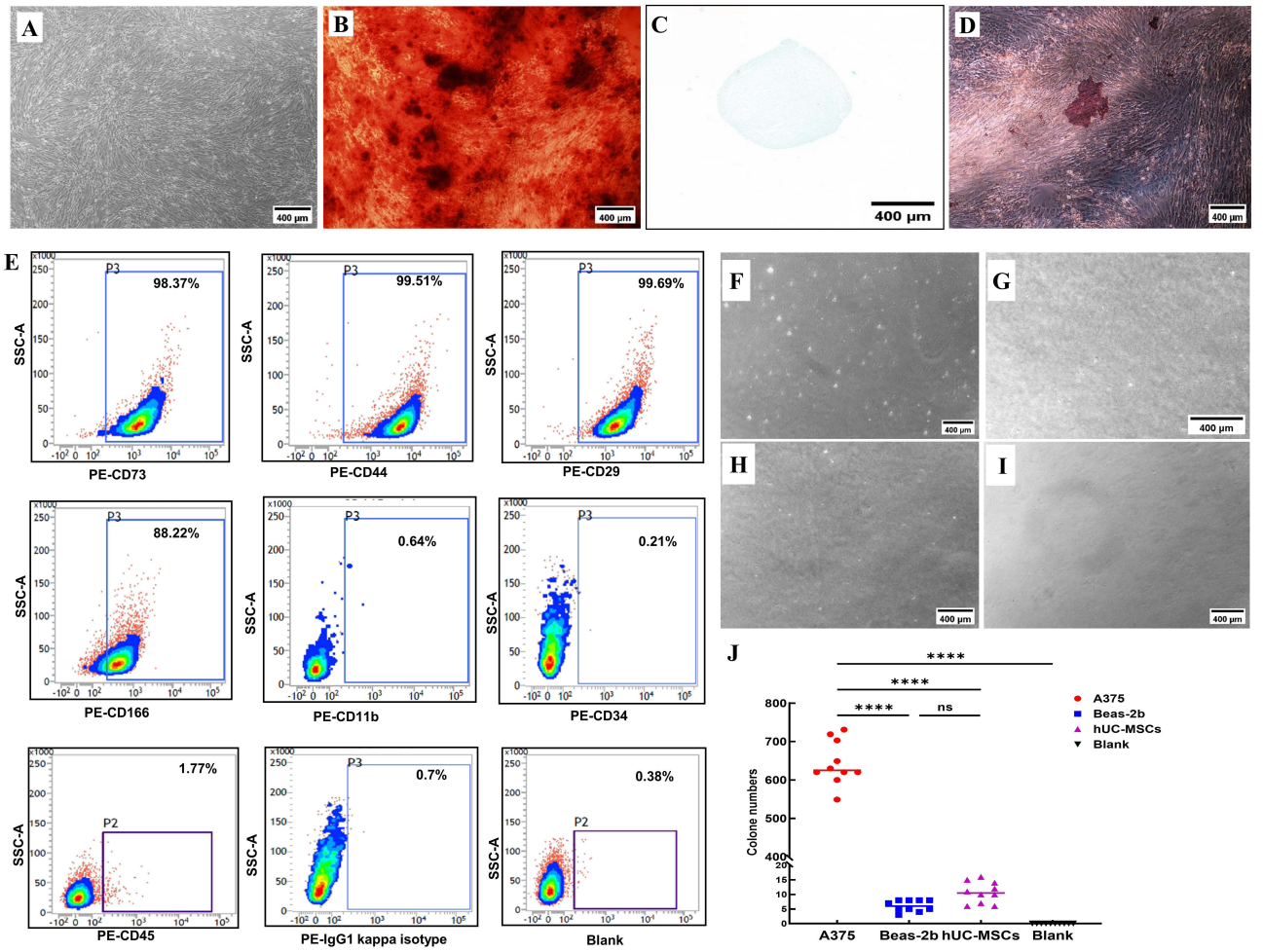

Figure 1 Phenotypic characteristics of hUC-MSCs.

Notes: (**A**) Light microscopic observation of hUC-MSCs (Passage 3), exhibiting long spindle-like morphology. (**B**) Alizarin red staining positive indicating osteogenic differentiation of hUC-MSCs. (**C**) Alcian blue staining positive indicating chondrogenic differentiation of hUC-MSCs. (**D**) Oil red-O staining positive indicating adipogenic differentiation of hUC-MSCs. (**E**) Flow cytometry examination indicating that the typical phenotype markers of hUC-MSCs were positive for CD73, CD44, CD29, CD166, while negative for CD11b, CD34, CD45, IgG1 kappa and blank. (**F**–**I**) Tumorigenic risk verifications ex vivo. A375 cells (Figure (**F**)) served as the positive control and Beas-2b cells (Figure (**G**)) as negative control. The hUC-MSCs (Figure (**H**)) were detected at the same time, and the completed medium (Figure (**I**)) was used as blank control. (**J**) Statistical analysis of ex vivo cloning formation. ****, $P<0.0001$, ns = no difference, one-way ANOVA analysis. Length of the scale bar = 400 μm.

Abbreviation: hUC-MSCs, human umbilical cord mesenchymal stem cells.

nm (Figure 2B and C). The zeta potential of Exos was measured at −4.25 ± 0.11 mV, while DiR-Exos had a range of was −12.6 ± 0.04 mV (Figure 2D and E). Western blot analysis confirmed that Exos derived from hUC-MSCs expressed surface markers of CD9, CD81, CD63, and TSG101 positively, while Calnexin was expressed negatively (Figure 2F).

NTA analysis determined that concentration of Exos was 1×10^7 particles/g per million cells. Therefore, the physical properties of Exos, including morphology, size distribution, zeta potential and surface antigen markers, were fully qualified.

Tumorigenicity and Sub-Acute Toxicity Assessment of Exos and hUC-MSCs in vivo

An overview of the tumorigenicity assessment procedure in vivo was provided, and the tumorigenicity risks of Exos and hUC-MSCs were assessed in tumor xenograft Crl:NU-Foxn1nu mice. (Figure 3A). No clinical signs of hair loss, or adverse reactions were observed in the PBS, hUC-MSCs, and Exos groups. Nude mice injected with A375 cells displayed a significant reduction in activity and response, with a visible tumor nodule at the injection site (Figure 3B). After 30 consecutive days of sub-acute toxicity observation, CT and MicroPET/CT imaging were performed on nude mice. Consistent with caliper measurement, the A375 group showed a significant increase in CT scanning and MV. On

https://doi.org/10.2147/IJN.S501843

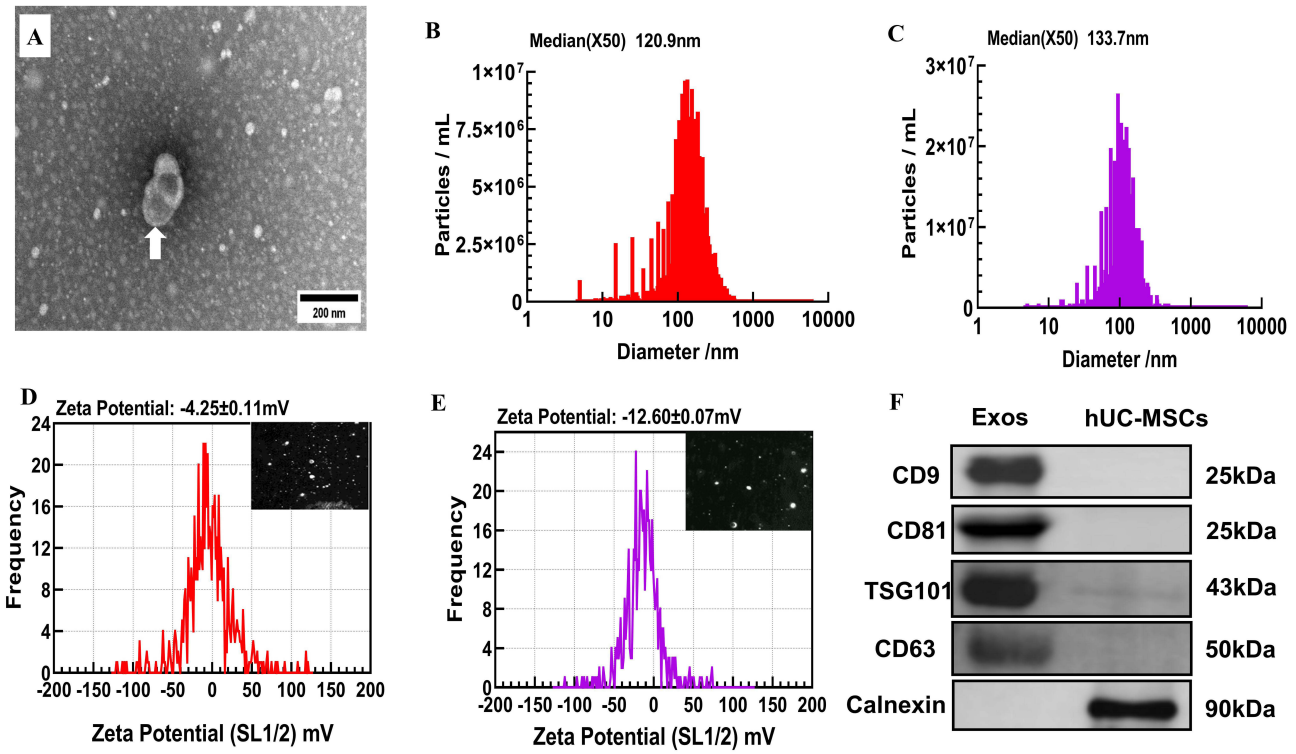

Figure 2 Characterizations of Exos and DiR-Exos.

Notes: (**A**) Exos identification by TEM as the white arrow indicated. Length of the scale bar=200 nm. (**B**) NTA examination of size distribution of Exos, revealing a median diameter of 120.9nm. (**C**) NTA examination of size distribution of DiR-Exos, revealing a median diameter of 133.7nm. (**D**) Zeta potential analysis and representative nanoparticle tracking imaging of Exos, revealing a zeta potential range of −4.25±0.11 mV. (**E**) Zeta potential analysis and representative nanoparticle tracking imaging of DiR-Exos, revealing a zeta potential range of −4.25±0.11 mV. (**F**) Western blot analysis of specific surface antigens from Exos and hUC-MSCs.

Abbreviations: Exos, exosomes; TEM, transmission electron microscopy; NTA, nanoparticle tracking analysis; DiR, 1.1'-dioctadecyl-tetramethylindotricarbocyanine iodide.

the other hand, Crl:NU-Foxn1nu mice processed with hUC-MSCs, Exos or PBS did not format tumor in the subcutaneous injection site. There was no MV detected among three groups (Figure 3C). To further explore the xenografts' glucose uptake on day 30 post-injection, ^{18}F-FDG MicroPET/CT imaging was conducted. A375 group exhibited the highest contrast agent uptake in both coronal and axial sections, compared to the other three groups (Figure 3D). While no contrast agent uptake was observed at the subcutaneous injection site in the other groups, the SUV_{max} and SUV_{mean} values for the A375 group were the highest, measuring 1.1429 and 0.9160, respectively (Figure 3E). In addition, no statistically significant differences were found in CT volume, metabolic volume, SUV_{max}, and SUV_{min} values among the Exos, hUC-MSCs, and A375 groups. This suggested that the A375 group exhibited a more robust metabolism at the tumor site compared to the other groups. After 30 days of treatment with hUC-MSCs or Exos, no significant increase in glucose, liver function markers, or kidney function markers was observed, suggesting minimal systemic side effects. In contrast, A375-treated nude mice exhibited elevated levels of GLU, LDH, AST and ALT markers compared to the three other groups (Figure 3F). Histopathological analysis revealed no signs of cell metastases or tumor formation at the injection site or in other organs in animals administered with PBS, hUC-MSCs, or Exos. Nevertheless, A375-treated mice exhibited fragmented cell nuclei in the kidneys, liver, tumor tissues, and lymph gland in the dorsolateral abdominal region. These fragmented cell nuclei were microscopically consistent with features of human malignant melanoma (Figure 3G). These findings supported the idea that hUC-MSC or Exos did not increase the risk of sub-acute toxicity or carcinogenesis in vivo.

Inhibition Telomerase Activity of Exos and hUC-MSCs

Telomerase activities of hUC-MSCs at P 8 under normoxic condition were 26.71%, while Exos showed 18.75%. Under hyperoxic conditions, telomerase activities of hUC-MSCs at P8 were 36.22%, and Exos were 24.12%. Compared to the

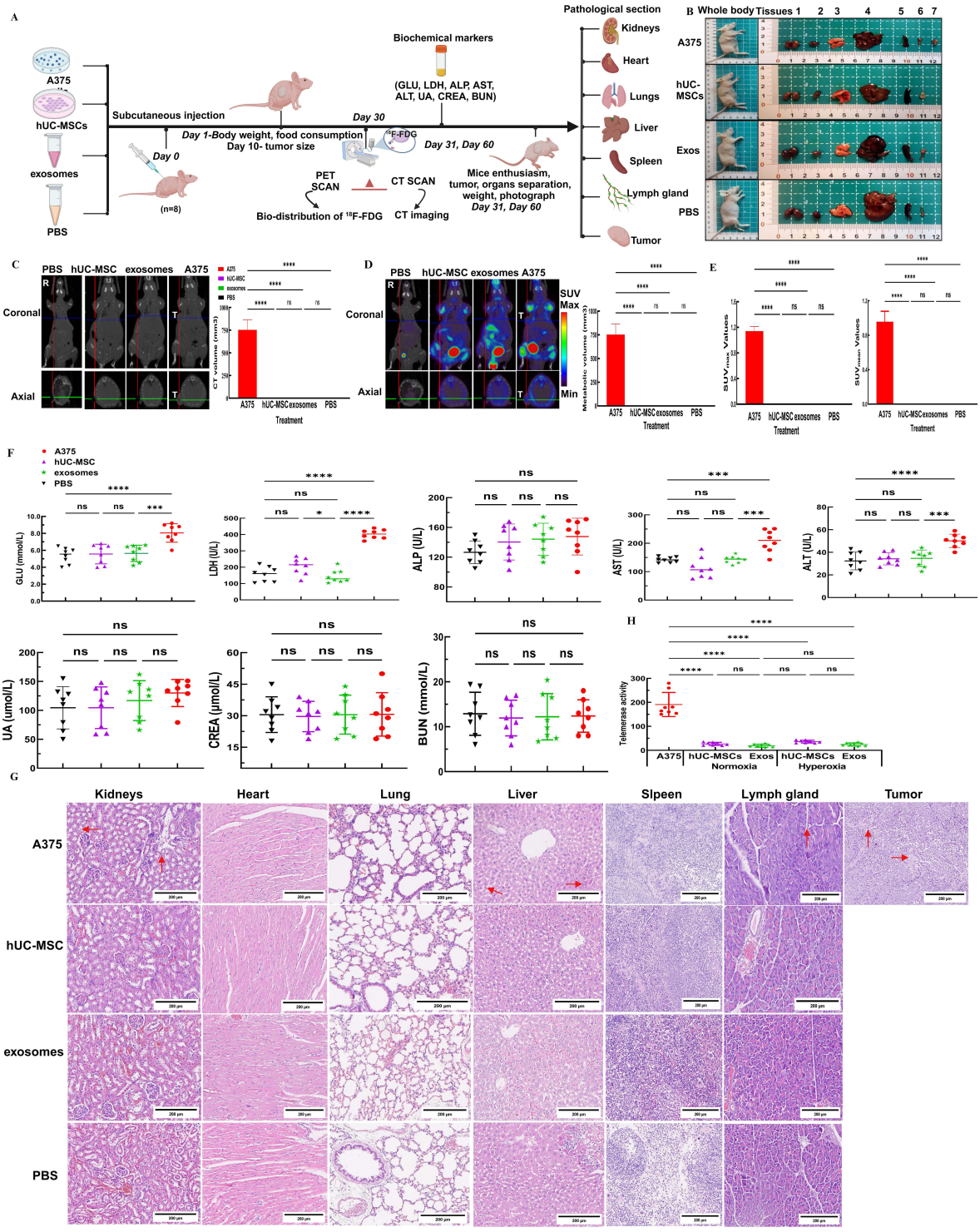

Figure 3 Subcutaneous tumor formation experiment in Crl:NU-Foxn1nu mice.

Notes: (**A**) Overview of the tumorigenicity assessment procedure in vivo. (**B**) Representative images of subcutaneous tumor formation from the whole body and main tissues of hUC-MSCs, Exos, and A375 for positive control, with PBS for negative control. 1: kidneys, 2: heart, 3: lungs, 4: liver, 5: spleen, 6: lymph gland, 7: tumor. (**C**) Representative coronal and axial sections of CT images for mice treated with PBS, hUC-MSC, Exos, or A375 along with CT tumor volume measurement on day 31. Intersecting lines represent subcutaneous injection location and T represents tumor. (**D**) Representative coronal and axial sections of ^{18}F-FDG PET-CT images of mice along with CT metabolic volume measurement on day 31 post-injection. Intersecting lines represent subcutaneous injection location and T represents tumor. (**E**) SUV_{max} and SUV_{mean} values of each group. (**F**) Measurement plasma indexes of GLU, LDH, ALP, AST, ALT, UA, CREA and BUN. n = 8 mice. (**G**) Pathological morphology of kidney, heart, lungs, liver, spleen, lymph gland, and tumor tissues from Crl:NU-Foxn1nu mice in PBS negative control, A375 positive control, hUC-MSCs, and Exos groups. Fragmented cell nuclei were indicated as red arrows. (**H**) Measurement of telomerase activity of cells in normoxia and hyperoxia conditions. Length of the scale bar=200 μm. n = 4 mice. Data are shown as mean ± SD. Statistical analysis of plasma indices among the four groups after vaccination, *vs PBS group. ***, P<0.001, ****, P<0.0001, one-way ANOVA analysis. Created in BioRender. Xu, W. (2025) https://BioRender.com/b59j337.

Abbreviations: SUV, standard uptake values; GLU, glucose; LDH, lactate dehydrogenase; ALP, alkaline phosphatase; AST, aspartate aminotransferase; ALT, alanine aminotransferase; CREA, creatinine; UA, uric acid; BUN, blood urea nitrogen.

https://doi.org/10.2147/IJN.S501843

A375 group, which served as a positive control, the telomerase activities were 190.86%. However, there was no statistical difference in telomerase activities between the normoxia and hyperoxia groups of hUC-MSCs and Exos (Figure 3H). TERT gene expression was consistently positive throughout the experiment, as indicated by the positive telomerase activity in A375 cells. These results showed that Exos or hUC-MSC did not induce carcinogenesis ex vivo.

Tumorigenicity and Chronic Toxicity Assessment of Exos and hUC-MSCs in vivo

Following A375 cells injection, the positive control group exhibited entirely different outcomes. Over the course of the observation period, body weight in the A375 group steadily decreased from day 18 to day 60 post-injection. In contrast, no noticeable changes in body weight or food consumption in the PBS, hUC-MSCs, and Exos groups (Figure 4A). A significant reduction in food intake was observed in nude mice injected with A375 cells from day 12 through day 60 (Figure 4B). Tumor volume in the A375 group increased steadily from day 10 to day 60 post-injection, whereas no signs of tumor formation were detected in the PBS, hUC-MSCs, and Exos groups (Figure 4C). No significant differences were observed between the PBS, hUC-MSCs, and Exos groups. However, organ coefficients of A375 group were obviously decreased in heart, lungs, liver, and pancreas (Figure 4D). Despite these changes, no significant alterations in glucose levels, liver function markers or kidney function markers were observed, indicating that almost no systemic damage occurred after 60 days of consecutive observation of the hUC-MSCs or Exos group. However, the A375-treated mice showed significantly higher levels of LDH, ALP, AST, ALT and UA markers compared to the three other groups. Additionally, glucose levels in the A375 group were lower than the other three groups at the 60-day post-injection examination (Figure 4E). Histopathological analysis at day 60 revealed fragmented cell nuclei in the kidneys, liver, tumor tissues, and lymph gland of the A375-treated mice, which were microscopically associated with malignant melanoma in humans. In contrast, no histopathological changes or cell metastases were observed in these organs of the PBS, hUC-MSCs, or Exos'-treated mice on the day 60 post-injection (Figure 4F). These results confirm the chronic biosafety and non-tumorigenic characteristic of Exos and hUC-MSCs in vivo.

Hyperoxic Exposure Inducing Lung Injury and Alveolar Simplification

The BPD mouse model was successfully established through hyperoxia-induced injury in this research. Dynamic changes in alveolar improvement were observed using light microscopy in neonatal mice on the PND 1, PND 3, PND 5, PND 7, and PND 14 under either normoxic or hyperoxic conditions (Figure 5A). From PND 3, the normoxic group showed no signs of inflammatory cell infiltration in the alveolar septa, congestion, hemorrhage, significant pulmonary edema, or the formation of hyaline membranes. In contrast, the hyperoxic group exhibited progressive inflammatory cell infiltration, noticeable pulmonary edema, the formation of hyaline membranes, and varying degrees of pulmonary congestion and hemorrhage in the alveolar septa. These inflammation and lung damage scores increased from PND 3 when exposed to sustained high oxygen conditions, reaching extreme severity by PND 14 (Figure 5B and C). As the alveoli of newborn mice developed and proliferated under normoxic conditions, secondary crest densities and MLI gradually increased from PND 5 to PND 14 (Figure 5E and G). Pulmonary alveoli of hyperoxia-exposed mice appeared simpler, with more uneven sizes, smaller RAC values (Figure 5D), larger alveolar cavities, and thinner alveolar walls (Figure 5F). Consequently, prolonged hyperoxia induced significant lung injury and alveolar simplification in the BPD mouse model.

General Health States of Normoxic or Hyperoxic Administration

The overall health status of the C57BL/6J mouse pups was based on body composition, milk intake, activity level, mental status and hair condition. In the hyperoxia, and the hyperoxia+GW4869 groups, the pups exhibited thinner bodies, reduced milk intake, dull hair, and decreased activity over time. Neurologic symptoms, including head tremors and gait instability, started to appear by PND 7 following oxygen exposure. However, the normoxic group displayed normal health with no unusual symptoms. The Exos group under hyperoxic conditions did not show any obvious abnormalities in body shape, milk consumption, or hair condition, although gait instability and head tremors persisted through PND 7 (Figure 6A). Between PND 1 and PND 3, body weights were similar across four groups. However, by PND 4, the normoxia group showed a significant increase in body weight compared to the hyperoxia and hyperoxia+GW4869 groups. From PND 5 to PND 14, no significant difference in body weight was observed between the normoxia and

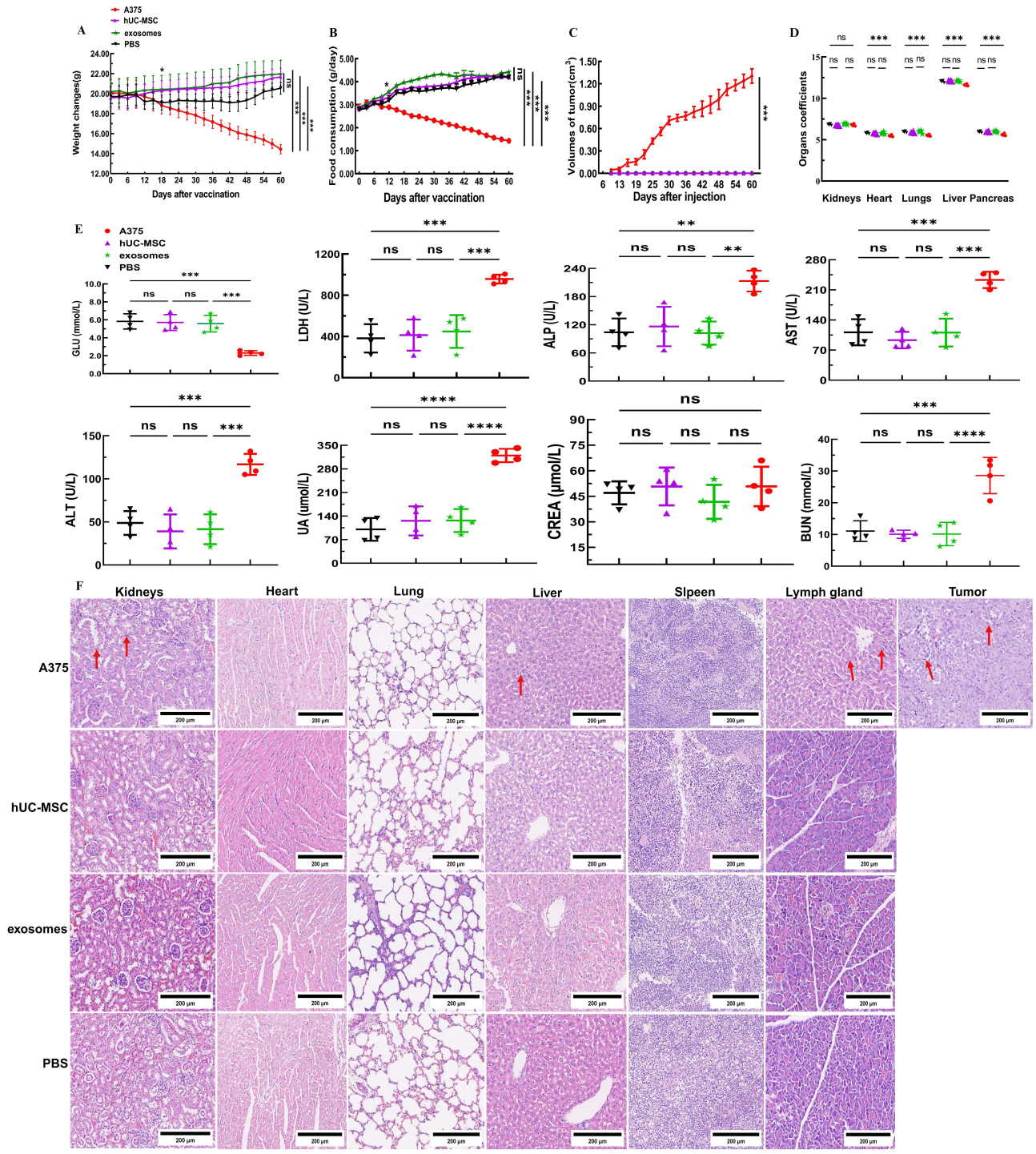

Figure 4 Safety evaluation of hUC-MSCs and Exos of chronic toxicity and tumorigenic impacts in vivo.

Notes: (**A**) Weight changes among four groups of Crl:NU-Foxn1nu mice over 60 consecutive days during treatments. (**B**) Food consumption changes. (**C**) Tumor volume changes. (**D**) Organ coefficient analysis. (**E**) Plasma indexes over 60 consecutive days (GLU, LDH, ALP, AST, ALT, UA, CREA and BUN). (**F**) Pathological morphology of major tissues after treatment over 60 days. Fragmented cell nuclei were indicated as red arrows. Length of the scale bar=200 μm. Statistical analysis of weight differences and food consumption among the four groups after vaccination, ns = not significant. *vs PBS group. ***, $P<0.001$, ****, $P<0.0001$, two-way ANOVA analysis. n = 4 mice. Created in BioRender. Xu, W. (2025) https://BioRender.com/m17h982.

hyperoxia+Exos groups. After 14 days of continuous oxygen exposure, the hyperoxia+GW4869 and hyperoxia groups had the lowest body weights, while the normoxia and hyperoxia+Exos groups had the highest, with statistically significant differences (Figure 6B).

https://doi.org/10.2147/IJN.S501843

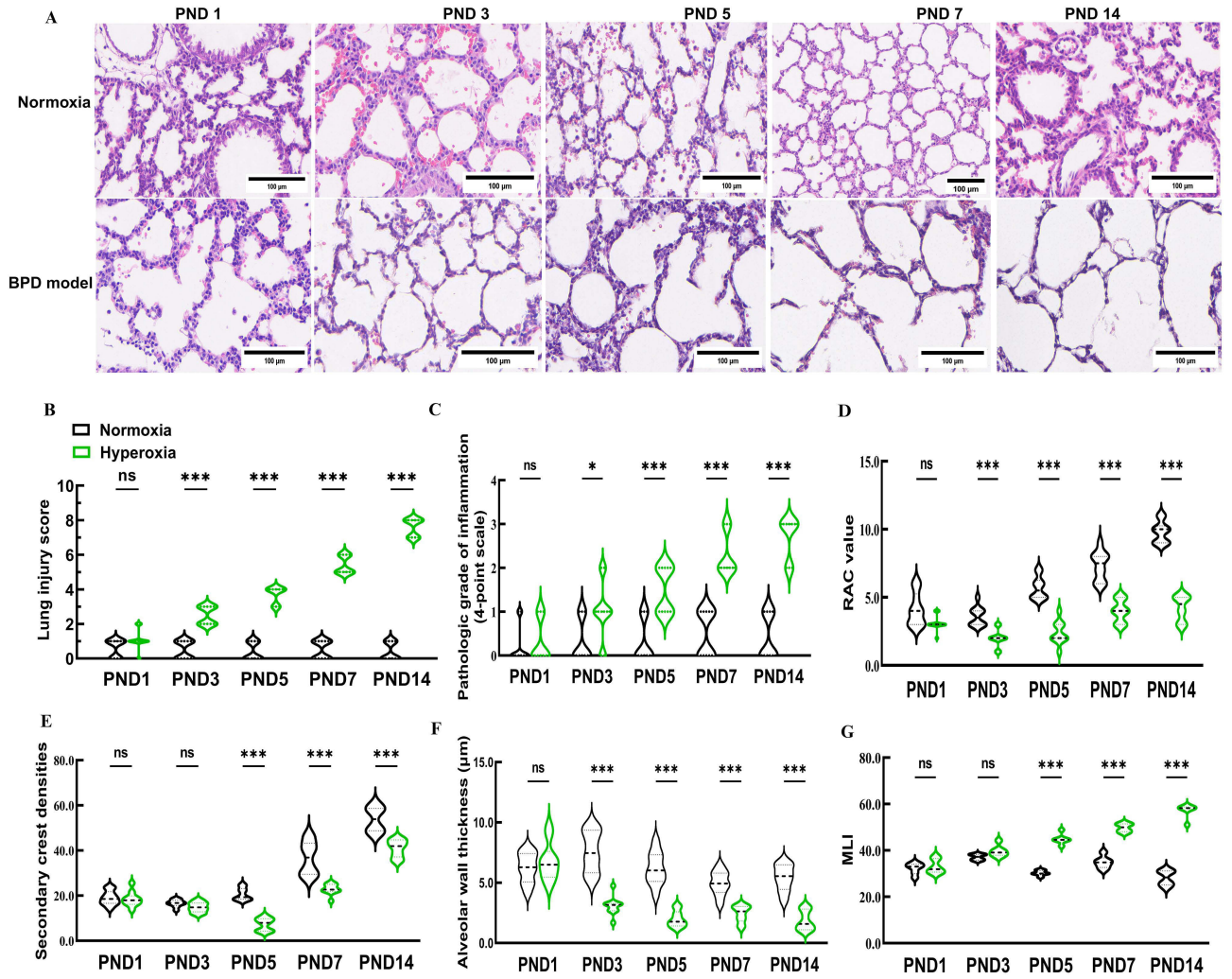

Figure 5 Establishment of hyperoxia induced BPD model on new-born C57BL/6J mice.
Notes: (**A**) Pathological morphology of alveolar changes in newborn mice with BPD model. (**B**) Lung injury score of normoxia and hyperoxia group. (**C**) Pathologic grade of inflammation of normoxia and hyperoxia group. (**D** and **E**) RAC values and secondary crest densities, which serve as indexes of the development of the pulmonary alveoli, were recorded. (**F** and **G**) Alveolar wall thickness and MLI were identified and documented as lung injury markers. Data were indicated as mean ± SD. * vs normoxia group. *, $P<0.05$. ***, $P<0.001$. Length of the scale bar=100 μm. n = 10 mice. Created in BioRender. Xu, W. (2025) https://BioRender.com/z03g659.
Abbreviations: BPD, bronchopulmonary dysplasia; RAC, radical alveolar number; MLI, mean linear intercept.

On PND 7, the body weight of the hyperoxia group and the hyperoxia+GW4869 group decreased compared to the normoxia group; however, no statistically significant difference in the body weight was observed in the hyperoxia+Exos group (Figure 6C). The survival rate of newborn pups exposed to prolonged hyperoxia was lower than that in the normoxic and hyperoxia+Exos groups. Specially, the survival rates of pups exposed to prolonged hyperoxia on the PND 1, 7, and 14 was 100%, 85.71%, and 51.43%, respectively. In the hyperoxia+GW4869 group, survival rates were 100%, 75%, and 20.83% on the PND 1, 7, and 14, respectively. Mortality in C57BL/6J mouse pups increased with prolonged exposure to hyperoxic conditions, but this was partially rescued by intranasal administration of Exos under hyperoxia. No pups died in the normoxia group or hyperoxia+Exos groups, whereas significant mortality was observed in the hyperoxia group and hyperoxia+GW4869 groups, indicating a statistically significant difference in survival rates (Figure 6D).

Exos Rescuing Hyperoxia-Induced Lung Injury and Alveolar Simplification

By nasal administration of Exos in hyperoxic conditions, C57BL/6J mouse pups showed reduced inflammatory cell infiltration in the alveolar cavity, improved hemorrhage and lung tissue congestion, relief of pulmonary edema, and enhanced alveolarization on the PND 7 and PND 14. In contrast, pups treated with GW4869 under hyperoxic conditions

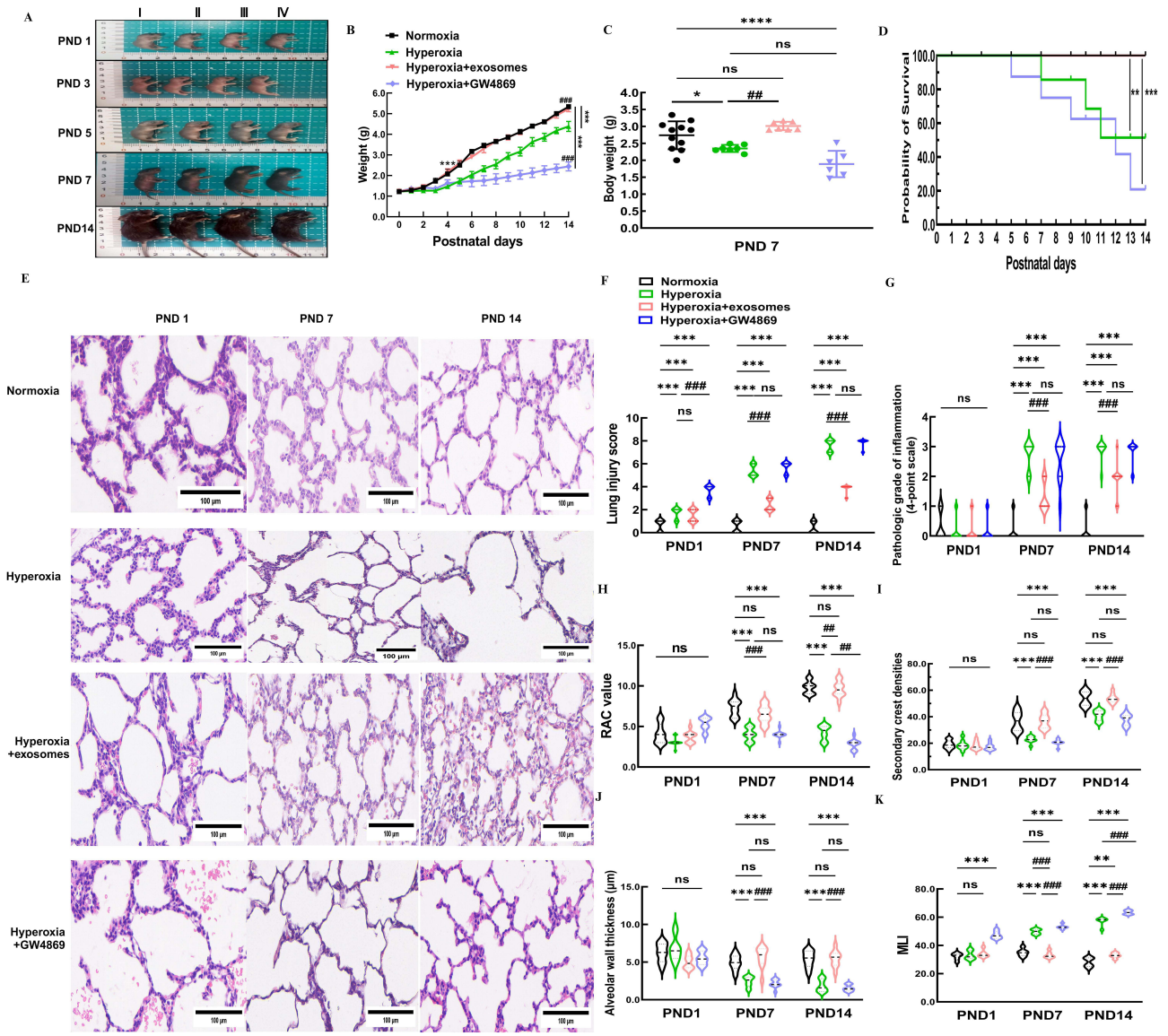

Figure 6 Pathological changes in alveolar of BPD mice after intranasal administration.

Notes: (**A**) Comparison of body shape between four groups of mice at PND 1, 3, 5, 7, and 14. I: normoxia group, II: hyperoxia, III: hyperoxia+Exos, IV: hyperoxia+GW 4869. (**B**) Weight changes in four groups of C57BL/6J mice over 14 consecutive days after birth. (**C**) Statistical analysis of weight differences among the four groups on PND 7. Data are shown as mean ± SD. *vs normoxia group. #vs hyperoxia group. *P<0.05, ****P<0.0001, ###P<0.01, ns = no difference. Ordinary one-way ANOVA analysis. (**D**) Survival rate of C57BL/6J mice for 14 consecutive days. (**E**) Representative pathological images of lungs of C57BL/6J mice after intranasal administration at different time point. (**F**) Lung injury score among four groups. (**G**) Pathologic grade of inflammation among four groups. (**H–K**) RAC value, alveolar wall thickness, MLI, and secondary crest densities were calculated in four groups from PND 1 to PND 14. Data are shown as mean ± SD.*vs normoxia group. #vs hyperoxia group. ***P<0.001, #P<0.05, ##P<0.01, ###P<0.001, ns = no difference, two-way ANOVA analysis. Length of scale bar = 100 μm. n = 10 mice. Created in BioRender. Xu, W. (2025) https://BioRender.com/v41v974.

Abbreviation: PND, postpartum day.

did not exhibit any improvements in inflammatory cell infiltration, pulmonary congestion and hemorrhage, or pulmonary edema (Figure 6E). Compared to the hyperoxia group, lung injury scores in the hyperoxia+GW4869 group began to increase from PND 1 and showed no statistical significance on the PND 7 or PND 14. However, the lung injury scores in the hyperoxia+Exos group were significantly lower on the PND 7 and PND 14 (Figure 6F). Furthermore, inflammation scores in the hyperoxia group started to increase from PND 7 to PND 14, with no statistical difference compared to the hyperoxia+GW4869 group. The hyperoxia+Exos group exhibited lower inflammation scores on the PND 7 and PND 14 compared to the hyperoxia group (Figure 6G). Thus, Exos administration effectively mitigated lung injury and inflammation induced by hyperoxia. RAC values, secondary crest densities, and alveolar wall thicknesses were all lower in the GW4869 group on PND 7 and PND 14 than the normoxia group (Figure 6H–J). In contrast, MLI in the

https://doi.org/10.2147/IJN.S501843

GW4869 group showed significant improvement on the PND1, 7 and 14 under continuous hyperoxic conditions (Figure 6K). These results confirmed that GW4869 administration did not enhance alveolarization or lessen lung damage. In comparison, Exos administration resulted in significant improvements in RAC, secondary ridge densities and alveolar wall thickness on the PND 7 and 14 (Figure 6H–J), while MLI was much lower (Figure 6K). The above results demonstrated that intranasal administration of Exos was an effective approach to alleviate hyperoxia-induced lung injury (HILI) and promote alveolarization in the BPD mouse models.

Exos Improving Lung Ventilation in μ-CT Tomography Construction

To complement the pathological analysis, all C57BL/6J neonates in the four groups underwent routine *μ-CT* scans; which were performed on PND 1, 3, 5, 7, and continued until PND 14. Representative sagittal, coronal, and axial sections of lung *μ-CT* images were displayed. In the *μ-CT* scan, air-filled regions such as the bronchi and alveoli appeared dark, while denser areas such as regions of inflammation, appeared brighter (Figure 7A). Additionally, 3D reconstruction models of lung tissue from C57BL/6J mice in the identical size range were listed (Figure 7B). The mean lung density of neonatal mice exposed to hyperoxia on PND 1 gradually increased compared to the normoxia group. Intranasal administration of Exos under hyperoxia conditions, however, markedly reduced the mean lung density from PND 3 to PND 14 compared to the hyperoxia group (Figure 7C). No statistically significant difference in total lung volume was observed on PND 1 among the four groups. Continuous exposure to high concentrations of oxygen, however, led to a reduction in pulmonary volume from PND 3 to PND 14, in contrast to the normoxia group. Exos intranasal administration under hyperoxia conditions rescued lung volume from PND 3 onward, whereas GW4869 administration did not reach a similar effect (Figure 7D). On PND 14, three distinct regions with different ventilation conditions in C57BL/6J mice were well matched with the visible structures on transverse CT scans, demonstrating the feasibility of this algorithm (Figure 7E). The oxygen levels in the normally ventilated regions of lung tissue in C57BL/6J mice were reduced after 14 days of hyperoxic exposure. Following intranasal administration of Exos, the proportion of pulmonary CT aerated volume that showed normal aerated regions was elevated compared to the hyperoxia group. In contrast, inhibition of Exos under hyperoxic conditions did not result in any increase in the normally ventilated lung tissue regions (Figure 7F). Statistical validation also confirmed these findings across all groups. The hyperoxia group showed more poorly aerated regions than the normoxia group. Exos administration alleviated these poorly aerated regions, whereas GW4869 did not show any improvement. Intranasal administration of Exos did not improve non-aerated regions under hyperoxia conditions (Figure 7G). These data supported the notion that regular intranasal administration of Exos under sustained hyperoxia could partially improve pulmonary ventilation of newborn C57BL/6J mice.

Bio-Distribution of Exos, DiR-Exos in vivo and ex vivo

PBS, Exos, or DiR-labeled Exos were administered intranasally into the nares of C57BL/6J mouse pups with BPD every other day from PND 1 to PND 14. DiR-Exos were used to investigate their bio-distribution and tracked non-invasively, both in vivo and ex vivo using IVIS images (Figure 8A). Under the same experimental conditions, DiR-Exos exhibited obvious fluorescence signals, which were not detected positively in the PBS or Exos group (Figure 8B). Fluorescence of DiR-Exos was predominantly localized in the abdomen within 24 hours after intranasal administration and continued to be present in the abdominal and thoracic regions until PND 14. This phenomenon, however, was not observed in the PBS or Exos groups (Figure 8C). The average fluorescence efficiencies of the DiR-Exos group increased gradually from PND 1 to PND 14, with a statistically significant difference observed compared to the Exos and PBS groups (Figure 8D). Fluorescence images confirmed that, following intranasal administration, DiR-Exos was predominantly present in lung tissues from PND 1 and continued to accumulate in the lung until PND 14. The primary organs of the PBS or Exos groups, however, showed almost no fluorescent signal ex vivo (Figure 8E). Lung tissue displayed the highest DiR signal from PND 1, 3, 5, 7, to 14, reinforcing the qualitative observations with quantitative data from ex vivo organ imaging (Figure 8F, H, J, L and N). The normalized fluorescence intensity indicated that DiR-Exos predominantly accumulated in lung, liver, kidney and heart at PND 1, 3, 5, 7 and 14 (Figure 8G, I, K, M and O). To the best of our knowledge, the bio-distribution of DiR-Exos in neonatal BPD mouse model is being examined for the first time both in vivo and ex vivo using routine intranasal administration.

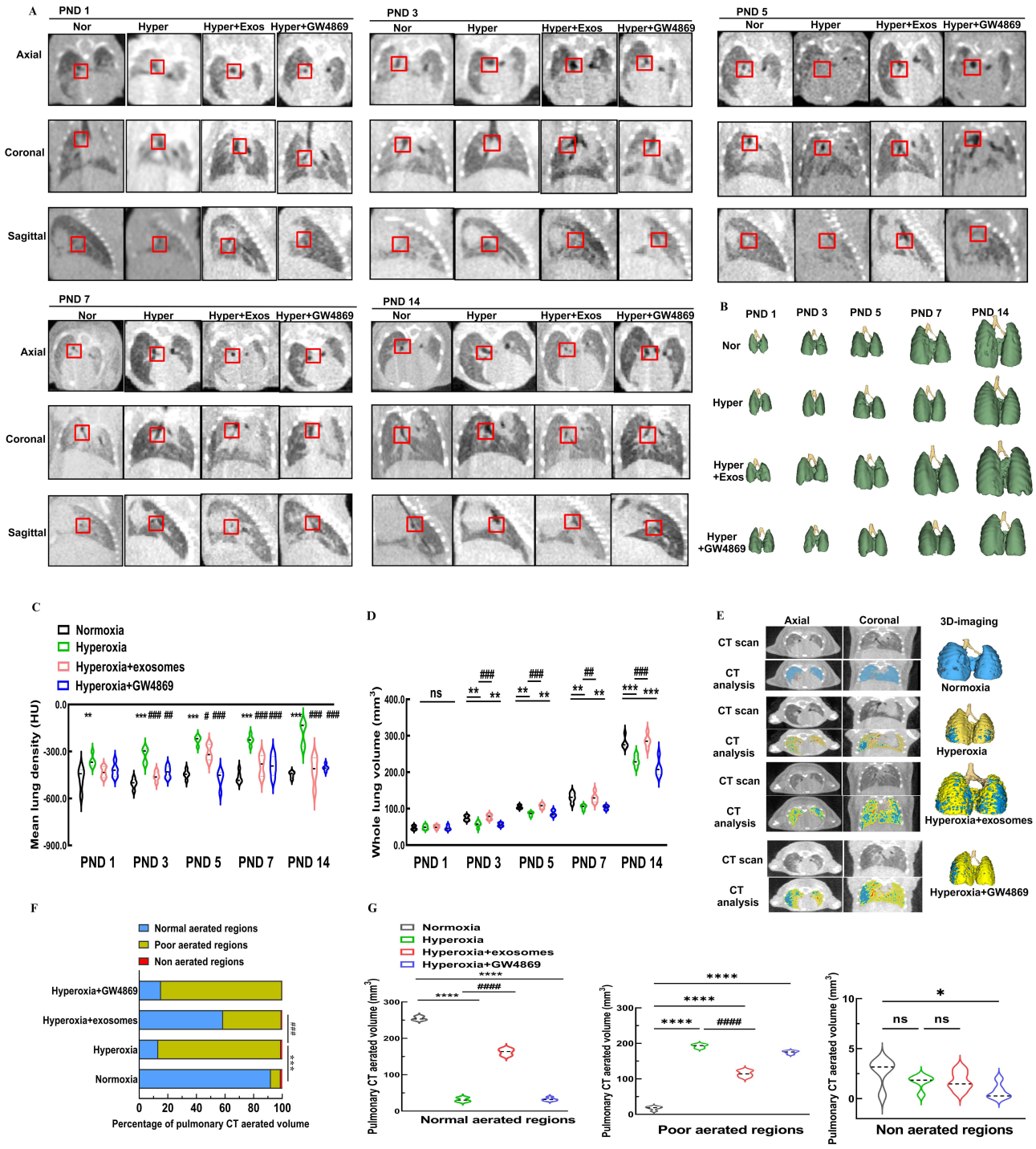

Figure 7 *μ-CT* images of lungs in newborn C57BL/6J mice with BPD.

Notes: (**A**) Axial, coronal and sagittal images were acquired at various time points, ranging from PND1 to 14. Bifurcation of right bronchi in newborn mice was recorded with a red square to make sure the same position was chosen in all images. (**B**) Representative images exhibited 3D reconstruction of the lungs of C57BL/6J mice at various time points, ranging from PND 1 to 14. (**C**) Mean lung density in HU. (**D**) Whole lung volume. Data were indicated as mean ± SD. * vs normoxia group. **, $P<0.01$. ***, $P<0.001$. # vs hyperoxia group, ## $P<0.01$, #### $P<0.001$. n = 5 mice. (**E**) Representative color maps and 3D reconstruction models of different ventilation areas in lung CT on PND 14. Blue represented normally aerated regions. Yellow represented poorly aerated regions. Red represented non-aerated regions. (**F**) Proportions of pulmonary CT aerated volume on PND 14. (**G**) Statistical analysis of pulmonary CT normal aerated regions, poor aerated regions, and non-aerated regions. Data were indicated as mean ± SD. #vs normoxia group, ##vs hyperoxia group, *$P<0.05$. ****, $P<0.0001$, ####$P<0.0001$, ns = no difference. Ordinary one-way ANOVA analysis. n = 5 mice. Created in BioRender. Xu, W. (2025) https://BioRender.com/e22k667.

https://doi.org/10.2147/IJN.S501843

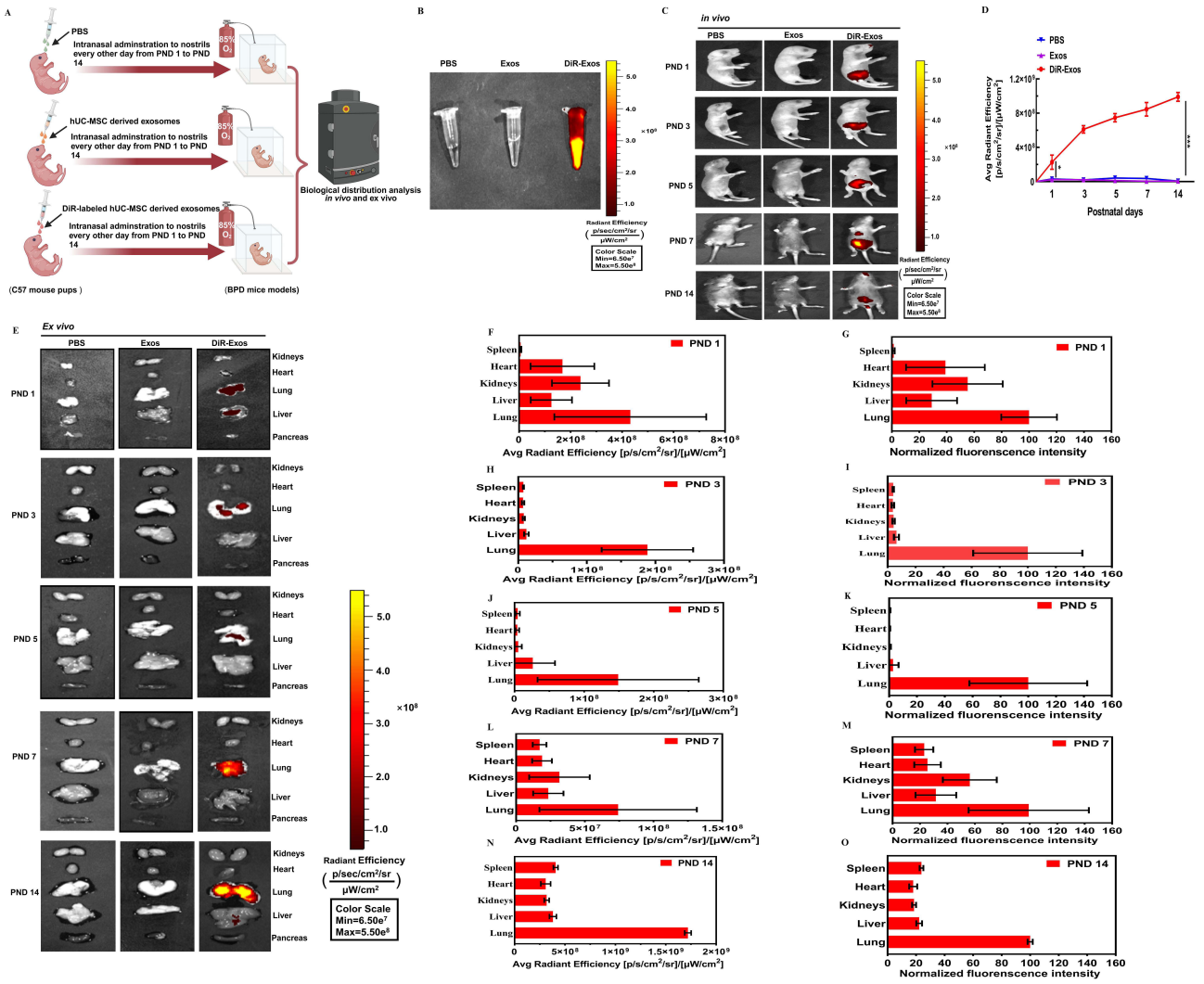

Figure 8 Fluorescence tracking of Exos in vivo and ex vivo.

Notes: (**A**) Workflow for tracking PBS, Exos or DiR-Exos in BPD mouse model in vivo. PBS, Exos, and DiR-labeled Exos were administered intranasally into nostrils of newborn C57BL/6J mouse pups, respectively. (**B**) Representative fluorescence images of PBS, Exos and DiR-Exos. (**C**) Typical fluorescence images on PND 1, 3, 5, 7, and 14 following intranasal delivery of PBS, Exos, or DiR-Exos in BPD mice model in vivo. (**D**) Average fluorescence efficiencies. Error bars were represented as mean ± SD, *vs normoxia group. *P<0.05, ****P<0.001, two-way ANOVA analysis. (**E**) Representative images of fluorescence organs on PND 1, 3, 5, 7, and 14 following intranasal delivery of PBS, Exos, or DiR-Exos in BPD mice model ex vivo. Organ notes were on the right side of panel. (**F, H, J, L** and **N**) Average radiant efficiency of organs of DIR-Exos on PND 1, PND 3, PND 5, PND 7 and PND 14. Figure 8 (**G, I, K, M** and **O**) Normalized fluorescence intensity of organs of DIR-Exos on PND 1, PND 3, PND 5, PND 7 and PND 14. Data were indicated as mean ± SD. n=5 mice. Created in BioRender. Xu, W. (2025) https://BioRender.com/r48b794.

Exos Restoring Pulmonary Capillaries and Endothelial Cells Components

TEM was used to observe the capillary lumen of C57BL/6J pups under normoxia on PND 14, revealing the presence of normal red blood cells (RBC) and thin blood-air barriers (BABs). Lamellar bodies (LB), intercellular tight junctions (Tjs), and microvillus (Mvs) at the cell apex were all observed in alveolar epithelial type II (AT2) cells (Figure 9A$_i$, A$_{ii}$). Long-term exposure to 85% oxygen disrupted the normal architecture of pulmonary capillaries, resulting in a collapsed capillary lumen, thickened, uneven BABs, and significant disruption of endothelial cell layer components. In AT2 cells exposed to hyperoxia, clear disruptions were evident, including endodermal detachment, relaxation of intercellular Tjs, absence of Mvs, and vacuolization of LBs (Figure 9B$_i$, B$_{ii}$). Exos administered intranasally under hyperoxia showed the recovery of thin BABs, a broad capillary lumen containing RBCs, and the interruption of the epithelial–mesenchymal transition in AT2 cells of recovering LB, Mvs, and Tjs (Figure 9C$_i$, C$_{ii}$). However, intranasal administration of GW4869 under hyperoxic conditions induced EMT in AT2 cells. This resulted in thicken BABs, a collapsed capillary lumen, and heterogeneously thick ECs (Figure 9D$_i$, D$_{ii}$). To quantify the ultrastructural alterations in the four groups, thicknesses of

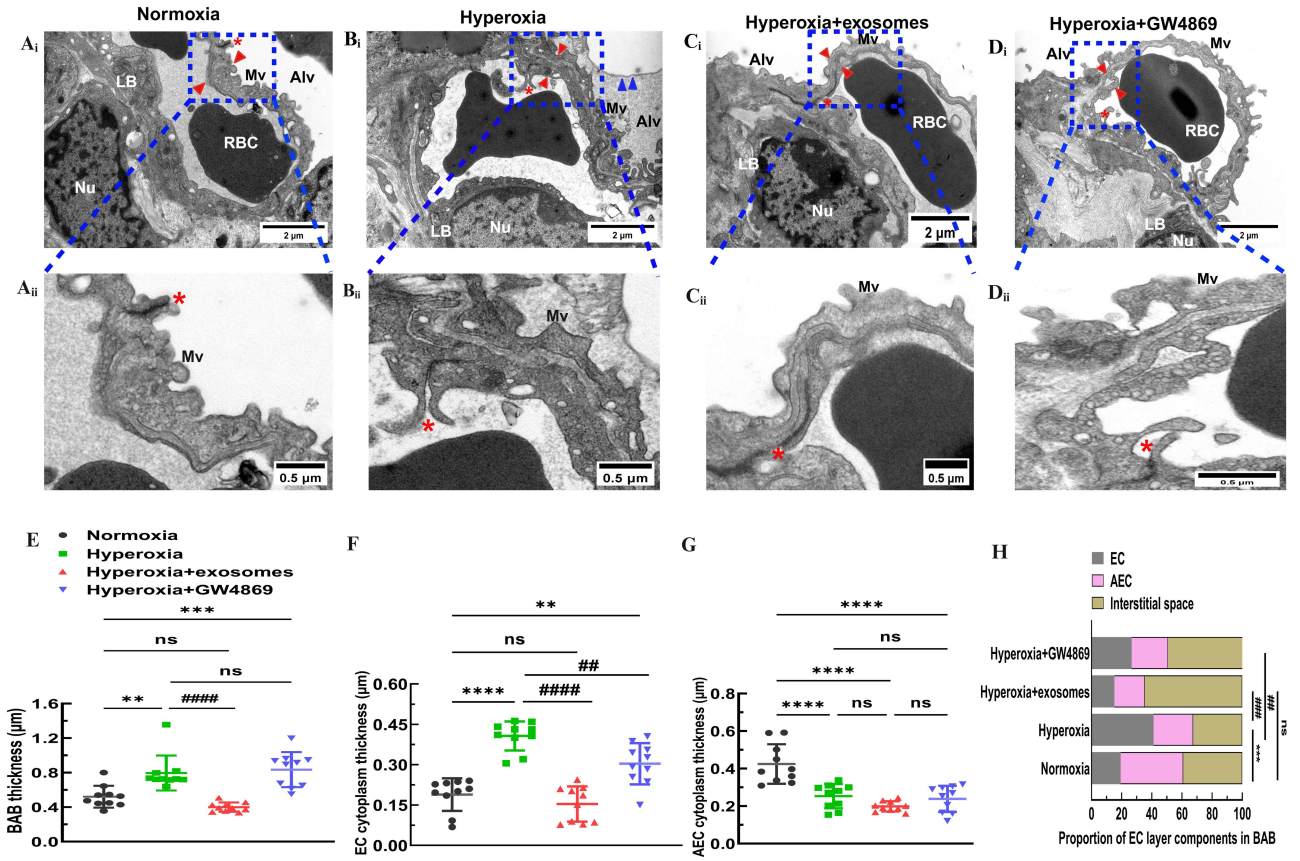

Figure 9 Representative images of TEM ultrastructure for ECs and AECs.

Notes: (**A_i**) Pulmonary capillaries and normal AT2 cells exhibited thin BABs, a broad capillary lumen with red blood cells inside, LB in the cytoplasm of AT2 cells, Mvs at the top of the cell, and intercellular Tjs under normoxic conditions in C57BL/6J mice lungs on PND 14. (**A_{ii}**) Under higher magnification, AECs, BM, and ECs were clearly differentiated into three layers in the BABs. (**B_i**) Pulmonary capillaries and AT2 cells displayed thick BABs, a collapsed capillary lumen, ECs with uneven thick cytoplasm, AT2 cells exhibited vacuolized LB, Mvs absence, relaxation of intercellular Tjs, and endodermal detachment under hyperoxic conditions in BPD mice lungs on PND 14. (**B_{ii}**) Under hyperoxic conditions, ECs occupied the majority of space, and BABs were thicker. (**C_i**) Pulmonary capillaries and AT2 cells presented thin BABs, a wide capillary lumen with red blood cells, recovery of LB, Mvs, and Tjs with repeated intranasal administration of Exos under hyperoxia on PND 14. (**C_{ii}**) Exos intranasally administered under hyperoxic conditions exhibited thinner BABs and ECs. (**D_i**) Pulmonary capillaries and AT2 cells displayed thick BABs, a collapsed capillary lumen, ECs with heterogeneously thick cytoplasm, vacuolized LB, Mvs at the top of the cell, and loose Tjs with repeated intranasal administered GW4869 under hyperoxia on PND 14. (**D_{ii}**) GW4869 intranasally administered under hyperoxic conditions resulted in heterogeneously thicker BABs and ECs. Length of scale bar (A_i, B_i, C_i, D_i) = 2μm. Length of scale bar (A_{ii}, B_{ii}, C_{ii}, D_{ii}) = 0.5μm. Red asterisk indicated intercellular tight junctions. Blue arrow head indicated endodermis cells. Red arrow head indicated blood-air barriers. (**E**) Mean value of BAB thickness of each group using ten different versions of field of each capillary. (**F**) Thickness of EC cytoplasm of each group. (**G**) Thickness of AEC cytoplasm of each group. (**H**) Proportion of EC layer components of each group. Data were presented as mean ± SD. $^{**}P<0.01$ compared to normoxia group, $^{***}P<0.001$, $^{****}P<0.0001$, $^{\#\#\#\#}P<0.001$ compared to hyperoxia group, n = 10 capillaries. Created in BioRender. Xu, W. (2025) https://BioRender.com/n03u632.

Abbreviations: EC, endothelial cells; AEC, alveolar epithelial cell; AT2, alveolar epithelial type II; BAB, blood-air barriers; LB, lamellar bodies; BM, basement membrane; Mvs, microvillus; Tjs, intercellular tight junctions.

BAB, EC, and AEC were measured. Intranasal Exos administration partially restored the normal BAB thickness, whereas these thicknesses in the hyperoxia and hyperoxia+GW4869 groups remained higher than in the normoxia group (Figure 9E). EC thicknesses in the hyperoxia and hyperoxia+GW4869 groups were significantly increased compared to the normoxia group, but the Exos intranasal administration was restored to the normal EC thickness (Figure 9F). Neither Exos or GW4869 administration restored normal AEC thickness, and the AEC thickness in the hyperoxia group was lower than in the normoxia group (Figure 9G). In the hyperoxia group, ECs were predominantly occupied in BABs; this proportion was restored in the Exos-treated group. Exos administration significantly improved the EC layer components in type II alveolar epithelial cells by reducing the proportion of EC layer components compared to the hyperoxia group (Figure 9H). In conclusion, intranasal Exos administration partially restored the structure of pulmonary capillaries by modulating the thickness of the BAB and the EC layer components in AT2 cells.

https://doi.org/10.2147/IJN.S501843

Exos Alleviating Inflammation Reactions

C57BL/6J mouse pups exposed to hyperoxia from PND 1 to PND 14 exhibited progressively higher levels of the pro-inflammatory cytokines CXCL-10, IL-1β, IL-6, and TGF-β1, compared to the normoxia group (Figure 10A–D). Nasal administration of Exos reduced the pro-inflammatory cytokine levels of CXCL-10, IL-1β, IL-6, and TGF-β1 compared to the hyperoxia group. Similarly, GW4869 under constant hyperoxic conditions also decreased the pro-inflammatory cytokines CXCL-10, IL-1β, IL-6, and TGF-β1 in C57BL/6J mouse pups on the PND 7 and PND 14, in contrast to the hyperoxia group (Figure 10E–H). Therefore, regular intranasal administration of Exos may help lessen inflammation reactions in the lungs of newborn mice with BPD.

Exos Repairing Pulmonary Vascular Injury and Disrupting Epithelial–Mesenchymal Transition

IHC analysis of lung tissue from newborn puppies revealed that the lungs failed to form secondary crests under hyperoxic conditions, leading to fewer and larger alveoli, simplification and uneven size of alveolar structures, and significant disruption of pulmonary vascular development, as evidenced by a decrease in CD31-stained vessels (Figure 11A and C). GW4869 administration halted pulmonary vascular development and reduced CD31 expression, with no significant differences from the hyperoxia group. In contrast, intranasal administration of Exos in hyperoxic conditions increased CD31 expression and improved pulmonary vascular density to near normoxic levels, suggesting that Exos may repair pulmonary vascular damage induced by in hyperoxia in C57BL/6J mouse pups (Figure 11C and F). The mesenchymal marker α-SMA was increased in the hyperoxia group, while epithelial markers such as E-cadherin and Twist1 were reduced compared to the normoxia group. Exos administration via the nasal route successfully reversed the hyperoxicity-induced decrease in E-cadherin and Twist1 and reduced α-SMA levels in lung tissue (Figure 11B, D and E). IHC results indicated that intranasal Exos treatment could repair lung vascular injury, promote vascular development, enhance epithelial marker expression, and reverse epithelial–mesenchymal transition caused by hyperoxia.

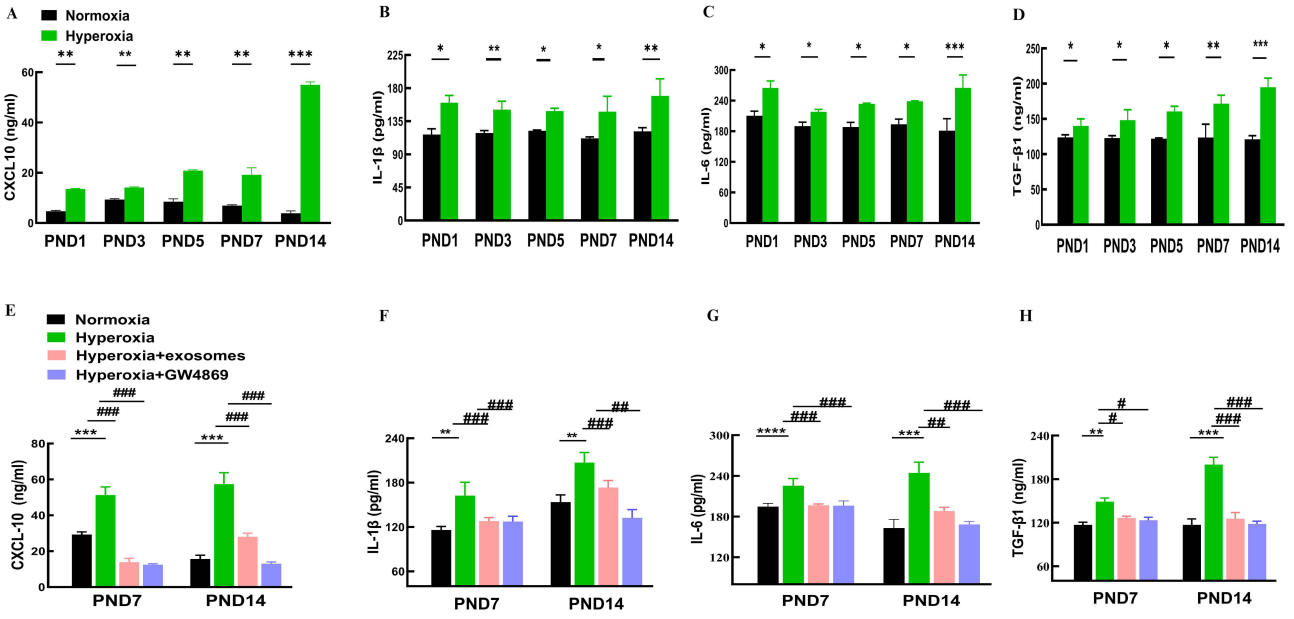

Figure 10 Inflammation cytokines levels in lung tissues in mice.

Notes: (**A–D**) CXCL-10, IL-1β, IL-6 and TGF-β1 levels of in the lung tissue among normoxia and hyperoxia groups ranging from PND1 to 14 were measured by ELISA. (**E–H**) CXCL-10, IL-1β, IL-6 and TGF-β1 levels of PND 7 and PND14 in the lung tissue among the normoxia hyperoxia, hyperoxia+Exos, and hyperoxia+GW4869 groups were measured by ELISA. All experiments were repeated at least three times. Data are shown as mean± SD.*vs normoxia group. # vs hyperoxia group. *P<0.05, **P<0.01, ***P<0.001, #P<0.05, ##P<0.01, ###P<0.001. n = 10 mice. Created in BioRender. Xu, W. (2025) https://BioRender.com/q61b238.

Abbreviations: CXCL-10, C-X-C motif chemokine 10; IL-1β, interleukin-1 beta; IL-6, interleukin-6; TGF-β1, transforming growth factor beta 1.

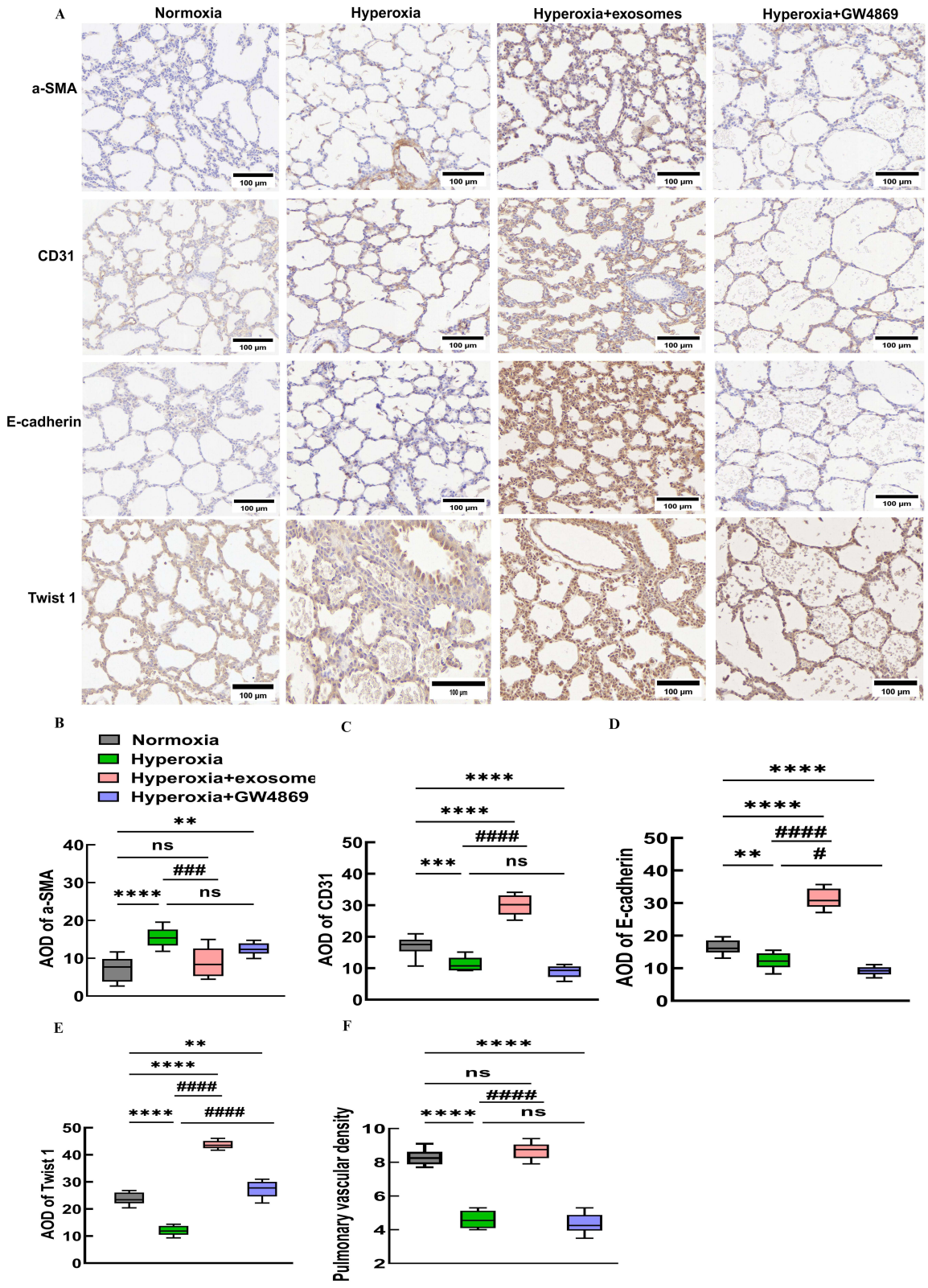

Figure 11 Immunostaining indicators of EMT and pro-angiogenic cytokines.

Notes: (**A**) IHC of α-SMA, CD31, E-cadherin, and Twist1 levels in C57BL/6J newborn mouse lung tissues. (**B-E**) AOD of α-SMA, CD31, E-cadherin, Twist1. (**F**) Pulmonary vascular density analysis. *vs normoxia group. #vs hyperoxia group. ***P<0.001, ****P<0.0001, #P<0.05, ###P<0.001, ####P<0.0001, ns = no difference, one-way ANOVA analysis. 400× magnification, scale bar=100μm. n = 10 mice. Created in BioRender. Xu, W. (2025) https://BioRender.com/u87f655.

Abbreviations: EMT, epithelial–mesenchymal transition; α-SMA, α-smooth muscle actin; AOD, average optical density.

https://doi.org/10.2147/IJN.S501843

Exos Reducing mRNA Expressions of Inflammation and Epithelial–Mesenchymal Transition Markers

The mRNA expressions of CD31, E-cadherin, Twist1, α-SMA, CXCL-10, IL-1β, IL-6, and TGF-β were evaluated on PND 14 lung tissues to assess lung vascular injury and the inducement of EMT. CD31, E-cadherin, and Twist1 mRNA expressions were lower in the hyperoxia group and higher in the Exos group. In contrast, the mRNA expression of aSMA was significantly higher under hyperoxic conditions than under normoxic controls, while it was lower in the Exos and GW4869 groups. CXCL10, IL-1β, IL-6, and TGF-β were all inflammatory cytokine mRNA expressions that were significantly higher in the hyperoxia group than in the normoxia group, while they were lower in the Exos group (Figure 12). Thus, Exos administration may reduce the inflammation of cytokines and disrupt epithelial–mesenchymal transitions in terms of mRNA expressions.

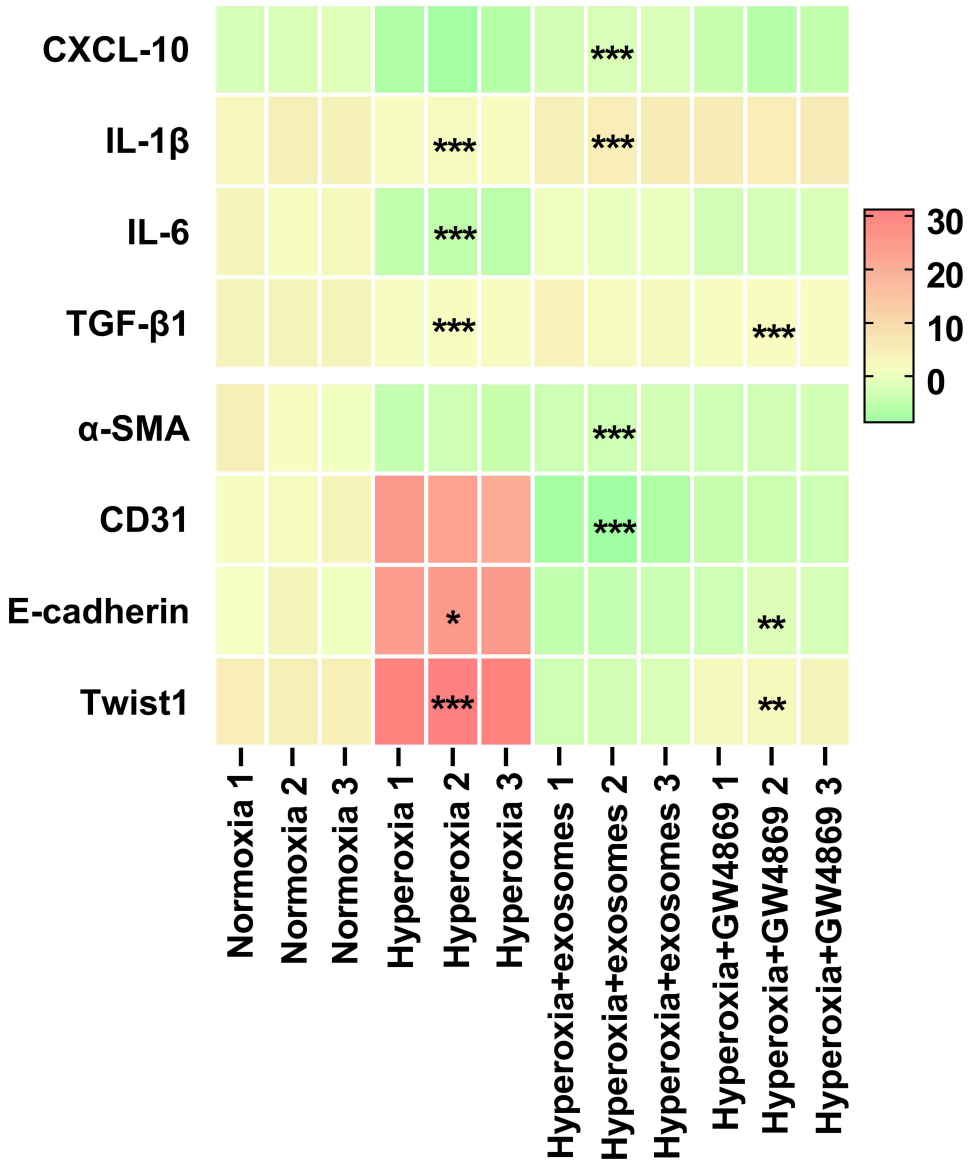

Figure 12 Heatmap representing mRNA expressions.

Notes: Based on RT-qPCR results, the mRNA expressions of the inflammatory cytokines CXCL-10, IL-1β, IL-6, and TGF-β1, as well as the EMT indicators α-SMA, CD31, E-cadherin, and Twist1 were measured in samples that were normoxic, hyperoxic, hyperoxic+exos, and hyperoxic+GW4869. ΔC_t values were presented. A higher C_t value indicated a lower mRNA expression. * vs normoxia group. *P<0.05, **P<0.01, ***P<0.001. Two-way ANOVA analysis. n = 3 mice.

Abbreviation: RT-qPCR, reverse transcription-quantitative polymerase chain reaction.

Discussion

This study aimed to investigate the potential therapeutic effects of Exos isolated from hUC-MSCs in a neonatal mouse model of BPD. It represents the first attempt to treat BPD in animals through the repeated intranasal administration of Exos. Our findings provide critical insights into the tumorigenicity risks associated with both Exos and hUC-MSCs. Key results include the promotion of alveolarization, restoration of efficient lung ventilation, recovery of pulmonary capillaries, bio-distribution of intranasally administered exosomes, disruption of EMT in alveolar type II cells, and the reduction of inflammatory cytokines, all of which contribute to the alleviation of HILI.

Human umbilical cord tissues are an ideal source of Exos, as they are readily available and free of ethical controversies, given that they are typically discarded as waste during childbirth. Additionally, hUC-MSCs exhibit a high proliferation rate and low immunogenicity, making them extensively used in clinical applications. In line with our findings, primarily cultured hUC-MSCs demonstrated typical characteristics, including adherence properties of adherent cells, multi-lineage differentiation potential ex vivo, expression of typical surface antigens as observed in flow cytometry analysis, and negative results in soft agarose colony formation assays. These findings are consistent with previous research.[42] Furthermore, our studies on Exos isolated from hUC-MSCs revealed fundamental features such as morphology, size distribution, zeta potential, and the expression of positive antigens.[43] To sum up, these properties make hUC-MSCs an excellent choice for the standardized production of Exos.

Tumorigenicity and toxicity are major concerns in Exos-based therapy, particularly involving hUC-MSCs origins. Telomerase activity, a key regulator of cancer, plays a pivotal role in tumor development and progression, being detected in over 90% of all tumor type.[44] Previous study demonstrated that the therapeutic effects of P3 hUC-MSCs were comparable to those of P8 hUC-MSCs but gradually diminished during long-term normoxic culture conditions.[45] In the current study, we examined the telomerase activity of P8 hUC-MSCs and Exos under normoxic and hyperoxic conditions. We found that telomerase activity remained stable during long-term hyperoxia treatment. Additionally, no positive hUC-MSC or Exos clones were detected in the soft agarose colony formation assay, indicating that long-term treatment inhibited tumorigenicity ex vivo. Regarding tumorigenicity and toxicity concerns in vivo, a previous study reported that the primary side effects of intravenously administering a high dose of hUC-MSCs at 50 million cells/kg included a 20% mortality rate, blood secretions from the urethra or oral-nasal regions, reduced food intake, and eventual respiratory and circulatory failure. No toxicity or adverse effects were detected at dose of 5×10^6 cells/kg in F344RG rats.[46] Another study showed that intravenous administration of a high-dose of hUC-MSCs at 3.0×10^7cells/kg exhibited transient coma, which could be eliminated by slow-speed infusion in cynomolgus macaque.[22] Subcutaneous injection of 0.5 mL of P4 hUC-MSCs with 1×10^9/L cell suspension in Balb/c nude mice did not produce toxic results after eight weeks of observation.[37] To prioritize animal welfare and prevent mortality, this study reduced the density of hUC-MSCs to a safer range. Subcutaneous injection of hUC-MSCs at doses up to 5×10^6 cells/kg or Exos 1.4×10^7 particles/g did not result in tumor formation in critical organs of either the Exos or hUC-MSC groups. No abnormal biochemical indices, clinical symptoms, or histological evidence of tumorigenic risk were observed. Further safety evaluations were performed in healthy Crl:NU-Foxn1nu mice. ^{18}F-FDG PET/CT scanning is a widely used technique for assessing the aggressiveness of malignant tumors. Both SUV_{max} and SUV_{min} have been utilized as prognostic factors for malignant tumors in earlier studies.[47] In this study, immunocompromised mice that underwent ^{18}F-FDG MicroPET/CT scanning showed no uptake of the contrast agent at the site of subcutaneous injection after one month. Mice in both the hUC-MSCs and Exos groups survived without significant abnormalities in body weight, food consumption, organ coefficients, or serum biochemical parameters. These findings demonstrate that the hUC-MSCs and Exos applied in this study are non-toxic and non-tumorigenic during sub-acute observation for 30 days in vivo. Furthermore, immunocompromised mice were also used as a model to test chronic tumorigenicity, as these animals are highly susceptible to the tumorigenic phenotype of positive control cell lines. The successful establishment of xenograft tumor models in vivo was confirmed by tumor formation at the injection site 10 days post-injection and by reduced body weight in the immunocompromised mice.[48] A previous study identified a diverse mutation spectrum in hUC-MSCs at different passages; however, no mutations associated with tumorigenic risk were detected based on whole-exome sequencing of high-frequency mutation analysis and subcutaneous tumorigenesis tests.[49] Among 12 hUC-MSC strains research demonstrated donor-dependent

heterogeneity in hUC-MSCs, yet no abnormalities in karyotype or tumorigenicity were found.[50] Our study confirmed that neither the hUC-MSCs nor Exos groups exhibited tumor formation in nude mice 60 days post-injection. Additionally, no histopathological abnormalities were observed in the main organs of either the hUC-MSC or Exos groups. These findings align with previous research confirming the long-term non-tumorigenicity of hUC-MSCs. Additionally, there was still no abnormal in glucose, liver or kidney function markers examined in the hUC-MSCs or Exos group, indicating the chronic biosafety of hUC-MSCs and Exos in vivo.

GW4869 was an inhibitor of Exos biogenesis and a noncompetitive nSMase2 inhibitor. Intraperitoneal administration of GW4869 in mice improved thoracic aortic calcification and nearly completely inhibited increased the mRNA transcription of osteogenic marker genes. These small extracellular vesicle (sEV) propagated miRNAs could serve as biomarkers and therapeutic targets for vascular calcification.[51] GW4869 was used to inhibit Exos release in mice and ex vivo, which accelerated senescence in both mice and cell types while confirming the essential role of Exos secretion by delaying aging.[52] GW4869 could also diminish the effects induced by Exos in M2 macrophages stimulating brown, beige fat differentiation in fibro adipogenic progenitors (FAPs) in vivo and ex vivo.[53] GW4869 effectively prevented the secretion of Exos in vivo by inhibiting the production of Exos, making it a powerful tool for studying Exos function. Thus, by using GW4869, we were able to elucidate the critical role of Exos in therapeutic efficacy. Inclusion of the GW4869 group allowed us to verify whether Exos are the primary mediators of therapeutic effects. As Exos played a role in treatment, we hypothesized that in the GW4869 group, the efficacy should be significantly diminished or absent due to the lack of Exos. Therefore, this group helped to demonstrate whether Exos play a key role in the therapeutic efficacy. For example, purified exosomes from NRK-52E cells activate rat kidney fibroblasts (NRK-49F) following hypoxic treatment. Inhibition of Exos by GW4869 treatment abolished NRK-49 cell activation and ameliorated renal fibrosis following unilateral ischemia reperfusion injury (UIRI) in vivo.[54] Considering that GW4869 could affect some normal physiological processes, we selected a dose of 2 μg for each administration in newborn mice, ensuring safe and non-invasive delivery. GW4869 acted as an inhibitor of Exos, allowing us to exclude the influence of factors other than Exos on the therapeutic effect. We also built up a hyperoxia control group to distinguish between the Exos effects and the possible non-specific interference caused by GW4869. The comparison between the GW4869 group and the Exos group under hyperoxic conditions was considered critical in this study. This comparison helps to confirm the specificity of the therapeutic effect of Exos, distinguishing it from other extracellular components or non-specific mechanisms. In our research, Exos administration restored lung injury and inflammation scores induced by hyperoxia; however, these improvements were interrupted by GW4869 treatment. As for alveolar simplification, Exos intranasal treatment recovered RAC values, secondary alveolar densities and alveolar wall thicknesses, reduced MLI injured by hyperoxia, and improved alveolarization. Nevertheless, the GW4869 treatment halted these improvements. GW4689 blocked the beneficial improvements of Exos on hyperoxia-induced alveolar development in mice, confirming the therapeutic effects of Exos when administered intranasally on pulmonary vascular and alveolar development under hyperoxia. The specific mechanisms were still required for further investigation.

MSCs have become a promising and potential treatment for BPD due to their natural ability to self-renewal, high efficiency in generating and replacing terminally differentiated cells, and their role in pulmonary vascular regeneration.[55] In a study involving four BPD patients, two intravenous doses of UC-MSCs at dose of 1×10^6 cells/kg patient body weight, administered 7 days apart, led to recovery from BPD without severe adverse effects.[56] However, another study reported intravascular infusion of MSCs led to pulmonary embolism at a high dose of 8×10^7 cells/kg in rats.[57] Additionally, the maximum tolerated dose of hUC-MSCs in mice was 2×10^7 cells/kg.[58] A phase -II clinical study suggested that the maximum hUC-MSC dose of intravenous infusion for premature infants is 5 million cells/kg, given their low weight and immature organ function.[59] Numerous studies have demonstrated that the paracrine effects of MSCs play a critical role in the treatment of BPD, particularly through Exos.[60,61] Compared to MSCs, Exos offer distinct advantages in mitigating hyperoxia-induced pulmonary damage, including immune tolerance, avoidance of microvascular blockage, and high efficacy in delivering therapeutic components.[62,63] Exos are inherently heterogeneous, primarily due to variations in their origins, isolation techniques, disease states, administration methods, dosage, and timing.[64,65] Many scientists believe that EVs have the potential to replace MSCs. A pre-clinical evaluation demonstrated that single and repeated intravenous administration of EVs at 30 μg protein to naive mouse showed a non-toxicity, and the bio-

distribution is major concentrated in liver, spleen and lung. EVs derived from hUC-MSCs could also alleviate lung injury and inflammation induced by lipopolysaccharide (LPS).[66] A previous study reported that intra-tracheal administration of Exos in a newborn Sprague-Dawley rats with BPD attenuated pulmonary hypertension, improved survival in a non-dose dependent manner, and a dose of Exos at 60×10^8 particles/g improved rats' survival. However, a set of EV-based preclinical studies on models of BPD verified that different doses required to be considered for cell treatment and EVs treatment, and optimal therapeutic dosage is still under exploring.[67] A safety dose study in cynomolgus monkeys reported that intravenous injection of Exos at a dose of 3.85×10^{12} particles did not result in obvious side effects on the general clinical conditions or Th1/Th2 cytokines.[35] In this study, Exos were used to treat BPD in place of hUC-MSCs, and their effects in vivo were studied. The Exos dose was calculated using the Experimental Zoology formula based on body surface area, resulting in a total of 1.4×10^7 particles/g administered multiple times in the neonatal BPD model.

The hallmark pathological features of BPD include impaired alveogenesis and angiogenesis.[68] In this study, we utilized BPD models of C57BL/6J mouse pups exposed to constant hyperoxic conditions. Lung development in mice is mostly finished by postnatal 2–3 weeks.[69] On PND 5, mice lungs were saccular and developed alveoli until PND 30.[70] Therefore, it is optimal to develop a short-term model by exposing mice to hyperoxia for 14 days to investigate hyperoxia-induced alveolar injury. This mouse model is widely used in BPD due to its similarity to the pulmonary-saccular developmental stages observed in preterm infants.[71–73] Our results indicated that neonatal C57BL/6J mice exposed to hyperoxia exhibited simplified alveolar structures, as evidenced by reduced RAC, lower secondary crest densities and alveolar wall thickness, along with increased lung injury scores and MLI. These findings were consistent with the hallmark pathological features of BPD, reinforcing the validity of our model in vivo. However, significant differences exist between mouse model and human preterm infants, making it difficult to achieve model of human BPD de novo. For example, the relatively simpler lung architecture in mice and the postnatal nature of their alveolarization process may not fully replicate the in utero development seen in premature infants. A recent single-cell RNA sequencing study firstly identified increased expression of *Acta1*+ and *Tubb3* in neonatal lungs. Further research might utilize transgenic mice for *Acta1*+*, Tubb3* or other specific genes in treating BPD.[71] While mechanisms of animal models in BPD remain valuable, further experiments are required to extrapolate findings to human premature infants. A review including 40 published studies using EVs as therapeutics in humans showed great heterogeneity in dosages due to route of administration and target disease.[74] The first prospective study of bone marrow MSC-EVs, referred to as ExoFlo, administered a single 15 mL intravenous dose (equivalent to 1.2×10^{12} particles) in 24 patients with COVID-19-related respiratory distress syndrome. This treatment improved the patients' oxygenation, reduced C-reactive protein and D-dimer levels, and was well-tolerated without any adverse events.[75] Subsequently, a prospective Phase II multicenter, double-blind, randomized, placebo-controlled trial reported that two 15 mL doses of ExoFlo, administered intravenously (equivalent to 1.2×10^{12} particles per dose), in 34 patients with moderate-to-severe COVID-related ARDS, reduced the duration of ventilation and mortality at day 60, without causing any adverse events. Overall mortality, duration of ventilation, and time to discharge all exhibited a dose-response trend favoring the high dose of ExoFlo.[76] Interestingly, Exos derived from human adipose-derived MSCs (haMSC-Exos) was reported to be safe and effective in treating severe COVID-19 through aerosol inhalation of Exos at 2.0×10^8 nano vesicles for consecutively 5 days.[77] Zofin, as a recently developed EVs-based therapy obtained from human amniotic fluid, has been subsequently used in the treatment of three patients with severe COVID-19, patients with post-COVID-19 symptoms, and patients with mild to moderate COVID-19 symptoms, with intravenous order of 10^{11} particles administered three or four times. Zofin treatment for COVID-19 patients, consisting of three or four intravenous doses of 10^{11} particles, demonstrated improvements in respiratory and general clinical symptoms, as well as reductions in inflammatory biomarkers, without adverse events.[78–80] In a phase II randomized, multicentric clinical trial conducted in Iran, COVID-19 patients with ARDS who received intravenous treatment with MSCs at dose of 100×10^6 cells followed by inhalation their released EVs at 8 μg per 1×10^6 cells, could effectively reduce circulating inflammatory markers, and were likely to reduce respiratory failure and death.[81] While both ExoFlo and Zofin were administered intravenously, inhalation haMSC-Exos at a quantitative range of $2–16\times 10^8$ particles showed good tolerability in healthy volunteers.[82] A large number of studies have demonstrated that BPD therapeutic dose of Exos in vivo was infected by multiple factors, such as sources, local or systemic administration mode, frequencies, and animal species. It was reported that standard therapeutic dose of EVs obtained from MSCs for treating BPD in animal

model ranging from 0.25×10^6 to 1×10^{10} particles, varying by up to about 400-fold.[83–86] Based on the findings of this study, followed by weight normalization and dose conversion using the body surface area, it is estimated that the total safe dose of exosomes for adults (assuming a body weight of 70 Kg) in the treatment of bronchopulmonary dysplasia (BPD) may be approximately 7.98×10^{10} particles. For infants (assuming a body weight of 3 Kg), the estimated total safe dose is 5.04×10^9 particles. These calculations provide an initial reference for potential clinical applications, and further experimental and clinical studies are necessary to validate these proposed doses to ensure their efficacy and safety.

Pulmonary CT analysis was widely used for the diagnosis, evaluation, and prognosis of premature infants and school-aged children.[87,88] Previous research demonstrated that structural pulmonary abnormalities and reduced lung volume were observed on CT scans of patients with BPD.[89] The primary manifestations of pulmonary structures on human CT images include regional heterogeneity, extensive pulmonary tissue remodeling, hyperinflation, and abnormal modifications of the pulmonary parenchyma.[90] In contrast to human BPD, pulmonary tissue damage in newborn mice within the BPD model, which involves continuous exposure to a high-oxygen environment, occurs uniformly. Therefore, it is crucial to investigate and evaluate newborn mice using *μ-CT* imaging in the context of the BPD model. Previous research has shown that neonatal mice exposed to high oxygen levels develop inflammation, pulmonary edema, collagen deposition, and fibroblast proliferation. These pathological changes can be effectively assessed using established acquisition parameters for *μ-CT* imaging.[40,91] Although *μ-CT* indicators, such as pulmonary volume and density, are considered primary markers in mouse models of lung diseases,[92] no study have investigated 3D lung reconstruction in newborn mice using a BPD model to explore pulmonary aeration. In this study, *μ-CT* scans were employed to monitor dynamic alterations in hyperoxia-associated lung changes in BPD mouse models following intranasal administration of Exos or GW4869. Using *μ-CT*, the mean lung density in the hyperoxia group was significantly higher compared to the normoxia group, but it decreased following regular Exos administration. Similarly, whole pulmonary volume and normally aerated regions were reduced in the hyperoxia group compared to the normoxia group, but were restored after regular intranasal administration of Exos. The effects of Exos could be halted by GW4869 administration. The findings from this study in the BPD model of newborn mice were partially consistent with results from previous studies.[91,93] As demonstrated by 3D reconstruction using established HU limit values, the innovative discoveries of this study primarily focused on the recoveries of lung volume and density following regular intranasal administration of Exos, as well as the effective improvement of lung ventilation regions. As natural macromolecular carriers, Exos could transport various bioactive molecules, bind to and internalize target cells, regulate pulmonary inflammatory responses, promote alveolar development, repair epithelial cell injuries and improve alveolar ventilation in BPD models. Exos may delay AT2 cells transdifferentiation by downregulating Wnt5a, which assisted to repair lung tissue of impaired alveolarization and improved alveolar ventilation.[94] As to anti-inflammatory responses, Exos enriched with TSG-6 could downregulate IL-1β, IL-6 and TNF-α expressions in the lung, inhibited proliferation and expression of macrophages, and promoted the phenotypic transition from M1 to M2. This process was mediated by TLR4/NF-κB signaling inhibition and STAT1/3 activation, which promoted AT2 cells viability and alveolarization in BPD.[95–97] In addition, Exos could promote endothelial cell proliferation, migration, tube formation, and pulmonary angiogenesis partially by elevating miR-185-5p targeted cyclin-dependent kinase 6 (CDK6) cascade, whereas miR200-a-3p overexpression had the opposite effects.[98,99] As for immune regulation, Exos may facilitate macrophages transition to M2 phenotype by inhibiting NF-κB p65 axis and stimulating STAT3 pathway.[100] MiR-335-5p from Exos inhibited MET TL14 expression, promoted m6A modification of integrinβ4 (ITGβ4), which inhibited glycolysis and alveolar epithelial cells inflammatory factors and finally alleviating pulmonary interstitial edema, inflammatory cell infiltration.[101,102] Previous study verified the critical role of angiogenesis in normal alveolarization, and dysfunction of vascular formation is one of the main features of BPD. CD31 acted as a communicated signal between epithelial and endothelial cells, therefore promoting angiogenesis.[103] Exos could upregulate von Willebrand factor (VWF) and CD31 receptor 1 (CD31R1) in endothelial cells. CD31R2 might also take part in alveolar capillary formation mediated by Exos.[62] Numerous research reported the positive effects of Exos on improving alveolar formation, lung tissues repairing, inflammation inhibition, and improving lung ventilation in BPD. In our research, intranasal Exos could arrived at lung within 24 hours, and promoting alveolar ventilation by increasing normal aerated regions reduced by hyperoxia, restoring mean lung density, and lung volume, which could be halted by

GW4869 inhibition. As for lung tissue repairing, impaired vascular development was further indicated by low CD31 expression, irregularly thinned BABs and ECs, and reduced pulmonary vascular densities. Regular intranasal administration of Exos every other day prevented neonatal mice exposed to hyperoxia from succumbing to lung injury. This treatment also increased alveolar wall thickness, RAC, and secondary crest densities. Moreover, Exos improved pulmonary vascularization under hyperoxia by upregulating CD31 expression, increasing pulmonary vascular densities, and restoring EC thickness within BABs. Conversely, the Exos inhibitor GW4869 disrupted these beneficial effects. These results demonstrated that persistent intranasal Exos administration is beneficial for treating BPD in vivo. A previous study indicated that damage to AT2 cells under hyperoxic conditions frequently induces EMT.[15] Additionally, EMT typically contributed to PF by inhibiting the proliferation of AT2 cells.[104] This study suggested that Exos could be administered intranasally to BPD models to effectively restore lung aeration, promote angiogenesis, and enhance alveogenesis. The findings further indicated that intravenous administration of Exos mitigated hyperoxia-induced lung damage by reducing inflammation and disrupting EMT on a regular basis. These results demonstrated that intranasal administration of Exos might play an important role in improving pulmonary ventilation in BPD mouse models, and mechanisms required discussion furtherly.

Exos could be delivered through various methods, such as intra-tracheal or intravenous administration, aerosol inhalation, or intraperitoneal injection. Optimal drug delivery methods were crucial for maximizing therapeutic efficacy while minimizing potential side effects.[83,105] These results also provided a new approach for treating BPD non-invasively using nano-vesicles. Intranasal delivery, a non-invasive and efficient administration method, is particularly advantageous for EVs as it avoids gastrointestinal breakdown and first-pass metabolism.[106] A recent study verified that intravenous injection and intranasal administration of hiPSC-Exos did not cause adverse effects on blood biochemical indicators.[107] Inhalation of secretome and Exos exhibited better therapeutic effects than MSC counterparts for promoting alveolar repair in silica-induced PF, with the dose standardized at 10×10^9 particles/kg in rats.[108] A previous study demonstrated that intranasal delivery of Exos could promote interleukin-10 (IL-10) production and protect mice from allergic asthma.[109] Additionally, intranasal administration of Exos has gained significant attention in the treatment of central nervous system disorders due to its ability to provide direct access to neural pathways and deliver therapeutic agents directly to the brain.[110] Previous research has demonstrated that plant-derived exosomes are often delivered to the respiratory system via intranasal administration for the treatment of pulmonary diseases. For the first time, BPD mouse pups were treated using this approach to evaluate the therapeutic effects of intranasal Exos on short-term HILI. The bio-distribution characteristics of intranasally administered Exos in vivo and ex vivo were also investigated.[111] Our findings align with the earlier research, showing that the average fluorescence efficiency of lung tissues labeled with DiR-Exos began to increase from PND 1. Furthermore, we discovered that repeated intranasal administration of Exos gradually increased lung tissue fluorescence efficiency, reaching its peak on PND 14. Variations in normalized fluorescence intensity and average fluorescence intensity of lung tissues may be attributed to differences in administration routes and animal models.[112,113] Another study found that intraperitoneal injection of MSCs or EVs was more effective than intravenous injection in reducing pulmonary damage and preventing microthrombus formation in blood vessels.[114] Thus, the non-invasive, non-cellular treatment of BPD through intranasal administration of Exos has shown promising potential. The findings of this study determined that the retention time of Exos in neonatal mice exceeded 48 hours. This information may provide valuable insights for optimizing the timing of intranasal administration in BPD mouse models.

Inflammation was a critical component of BPD and played a key role in regulating lung matrix remodeling. Recent study demonstrated that prolonged exposure of neonatal mice to high oxygen levels activates macrophages through IL-6 signaling.[95] Furthermore, alveolarization and pro-fibrotic lung remodeling were disrupted by CXCL10-driven macrophage chemotaxis via CXCR3 signaling.[115] TGF-β was secreted and stored in the extracellular matrix, while IL-1β was secreted by activated lung macrophages. Both cytokines were key inflammatory mediators that disrupt alveolar development in BPD.[116,117] There were three different sub-types of TGF-β, namely TGF-β1, TGF-β2, and TGF-β3, each exhibiting different temporal expression patterns during pulmonary development in animals. TGF-β1 was typically expressed during the early saccular stage of lung development, and its proper expression was crucial for normal early lung maturation.[118] Additionally, guanine nucleotide-binding proteins Gαq/11 played a crucial role in the spatial regulation of lung development in mice by mediating integrin-dependent TGF-β activation in lung epithelial cells. The MSC-specific deletion of Gαq/11 also affected lung development in mice, leading to increased MLI, unevenly enlarged alveolar cavities, reduced secondary crest densities, and abnormal pulmonary

vascular by PND 14.[119] This phenotype was similar to BPD. Multiple studies reported that hyperoxia induced overexpression of TGF-β. Mouse pups exposed to a high oxygen concentration of 85% from the PND 1 to PND 20 showed increased TGF-β1 expression throughout alveolar development, along with elevated pSmad2/pSmad3 levels. Notably, a intraperitoneal administration of TGF-β neutralizing antibody reduced Smad2/Smad3 phosphorylation and significantly improved alveolarization and elastin deposition.[120] Additionally, TGF-β1 was essential for PF development, acute lung injury, as well as ventilation induced lung injury (VILI). By activating TGFBR1, TGF-β1 regulated JAK/STAT, Smad, MAPK, Wnt, and ERK signaling pathways, and promoting the development of EMT in PF.[121] TGF-β1 was up-regulated after high positive end-expiratory pressure (PEEP) ventilation and associated with the occurrence of alveolar capillary leakage.[122] TGF-β1 overexpression in the first week of the lung primarily impacted lung injury-related symptoms such as pulmonary edema, alveolar collapse, decreased alveoli surface density and fibrotic septal wall remodeling. Gene transfer to the respiratory system, downregulated proteins, and elevated surface tension were also followed.[123] In our study, up-elevated expression of TGF-β1 was also observed in the hyperoxia group, and the pathological characteristics in lungs were consistent with BPD mouse models on PND 7 and PND 14, with lessening alveolar densities, RAC values, and secondary crest densities. Previous study reported that MSC infusion could reduce pro-inflammatory cytokine levels and promoted pulmonary development and vascularization in mouse models.[124] The hAMSCs administration attenuated EMT in PF by delivering miR-181a-5p, which downregulated TGFBR1. This process promoted epithelial cell proliferation and alleviated epithelial cell apoptosis through paracrine effects.[125] MSCs also inhibited the expression of TGF-β1, increase the activity of downstream epithelial Na^+ channel (ENaC), PI3K/AKT, and Rac1 signaling pathways, and repair deleterious tissue conditions in BPD animal models.[126] IL-1β was identified as one of the central cytokines in the disease-associated networks in BPD. Hyperoxia exposure increased IL-1β expression in both blood serum and bronchoalveolar lavage fluid, contributing to lung inflammation and the development of BPD.[127,128] In LPS-induced BPD animal models, activation of the NOD-, LRR- and pyrin domain-containing 3 (NLRP3) inflammasome was related to BPD developing, characterized by increased caspase-1 activation, elevated IL-1β levels, inflammation, and decreased alveolarization.[129] Caspase-1 could activate pro-IL-1β, turning them into mature proinflammatory cytokines. Simultaneously, caspase-1 cleaved and activated gasdermin D (GSDMD) pores, which not only permitted the influx of water and ions but also led to lytic cell death, a pro-inflammatory form of programmed cell death known as pyroptosis. The GSDMD pores allowed the release of IL-1β into extracellular space, which alleviated inflammation and disrupted alveolarization.[130] Additionally, blocking IL-1β by IL-1 receptor antagonist (IL-1ra) or inhibiting the NLRP3 inflammasome by glyburide in hyperoxia-exposed mice led to reduced inflammation and improved alveolarization. Ventilated preterm baboons showed activation of NLRP3 inflammasome, accompanied by an elevation in IL-1β: IL-1ra ratio. The IL-1β:IL-1ra ratio in tracheal aspirates from preterm infants with respiratory failure serves as a predictor for the development of BPD.[131] In BPD rats, Exos treatment could promote pulmonary vascular remodeling, alleviate the abnormality of IL-1β, alleviate the abnormality of IL-1β, and improve alveolar densities.[61] Our study confirmed that regular intranasal administration of Exos effectively reduced expressions of TGF-β and IL-1β on PND 7 and 14 in mice models, rescuing lung injury and inflammation scores caused by hyperoxia while increasing alveolar density, RAC values, and secondary crest densities. However, these effects were inhibited by GW4869 inhibition.

Limitations

Despite the promising results, this study has several limitations. First, the intranasal administration of Exos, although the pulmonary prognosis was significant.[132] Future research could focus on improving Exos utilization efficiency in pulmonary tissue following a single intranasal administration. Additionally, inter-donor variations could not be assessed due to the limited sample size of hUC-MSCs used in this investigation. Standardized quality studies involving both Exos and hUC-MSCs are necessary to confirm these findings further. Genetic analysis of tumorigenic risks of Exos and hUC-MSCs is suggested. Lastly, pulmonary pathology changes were evaluated in the BPD mouse model only up to PND 14. Future preclinical research should comprehensively investigate the long-term effects and potential adverse outcomes of intranasal Exos administration for BPD treatment.

Conclusion

In summary, our study is the first to confirm the therapeutic efficacy and bio-distribution of repeated intranasal administration of Exos in neonatal BPD mice models, which might repair hyperoxia induced pulmonary injury via

improving effective ventilations of lung tissue, promoting pulmonary alveolar simplification, rescuing pulmonary capillaries, decreasing inflammatory cytokines and interrupting EMT. Athymic nude mice at a single dose of 5×10^6 cells/kg of hUC-MSCs or 1.4×10^7 particles/g of Exos exhibited no obvious toxicity and tumorigenicity during 60 days of consecutive observation. In consequence, our research sheds light on a nano-based non-cellular, non-invasive treatment of BPD at a safe dose, providing a potential strategy for BPD therapy.

Data Sharing Statement

All the original data presented in this research are illustrated in the manuscript and supplementary materials. Further inquiries can be contacted directly to the corresponding author.

Acknowledgments

Figures in this manuscript were created using BioRender software, https://biorender.com/. The Graphical Abstract was Created in BioRender. Xu, W. (2025) https://BioRender.com/b15q303.

Author Contributions

All authors made a significant contribution to the work reported, whether that is in the conception, study design, execution, acquisition of data, analysis and interpretation, or in all these areas; took part in drafting, revising or critically reviewing the article; gave final approval of the version to be published; have agreed on the journal to which the article has been submitted; and agree to be accountable for all aspects of the work.

Funding

This study was supported by grants from projects of Wu Jieping Medical Foundation Clinical Research (No. 320.6750.2023-24-10) and the National Natural Science Foundation of China (No. 82371710).

Disclosure

The authors report no conflicts of interest in this work.

References

1. Kato S, Iwata O, Kato H, et al. Furin regulates the alveolarization of neonatal lungs in a mouse model of hyperoxic lung injury. *Biomolecules*. 2023;13(11):1656. doi:10.3390/biom13111656
2. Zini T, Miselli F, Berardi A. Noninvasive monitoring strategies for bronchopulmonary dysplasia or post-prematurity respiratory disease: current challenges and future prospects. *Children*. 2023;10(11). doi:10.3390/children10111753
3. Yang M, Chen Y, Huang X, et al. ETS1 ameliorates hyperoxia-induced bronchopulmonary dysplasia in mice by activating Nrf2/HO-1 mediated ferroptosis. *Lung*. 2023;201(4):425–441. doi:10.1007/s00408-023-00639-1
4. van de Loo M, van Kaam A, Offringa M, et al. Corticosteroids for the prevention and treatment of bronchopulmonary dysplasia: an overview of systematic reviews. *Cochrane Database Syst Rev*. 2024;4(4):CD013271. doi:10.1002/14651858.CD013271.pub2
5. Silveira RC, Panceri C, Munoz NP, et al. Less invasive surfactant administration versus intubation-surfactant-extubation in the treatment of neonatal respiratory distress syndrome: a systematic review and meta-analyses. *J Pediatr*. 2024;100(1):8–24. doi:10.1016/j.jped.2023.05.008
6. Roehr CC, Farley HJ, Mahmoud RA, et al. Non-invasive ventilatory support in preterm neonates in the delivery room and the neonatal intensive care unit: a short narrative review of what we know in 2024. *Neonatology*. 2024;121(5):576–583. doi:10.1159/000540601
7. Jensen EA, Wiener LE, Rysavy MA, et al. Assessment of corticosteroid therapy and death or disability according to pretreatment risk of death or bronchopulmonary dysplasia in extremely preterm infants. *JAMA Netw Open*. 2023;6(5):e2312277. doi:10.1001/jamanetworkopen.2023.12277
8. Enzer KG, Baker CD, Wisniewski BL. Bronchopulmonary dysplasia. *Clin Chest Med*. 2024;45(3):639–650. doi:10.1016/j.ccm.2024.03.007
9. He Y, Zhang M, Tang J, et al. A retrospective cohort study on mortality, morbidity, and care practices for 1750 very low birth weight infants, 2016-2021. *Chin Med J*. 2024. doi:10.1097/CM9.0000000000002923
10. Bell EF, Hintz SR, Hansen NI, et al. Mortality, in-hospital morbidity, care practices, and 2-year outcomes for extremely preterm infants in the US, 2013-2018. *JAMA*. 2022;327(3):248–263. doi:10.1001/jama.2021.23580
11. Doyle LW, Ranganathan S, Mainzer RM, et al. Relationships of severity of bronchopulmonary dysplasia with adverse neurodevelopmental outcomes and poor respiratory function at 7-8 years of age. *J Pediatr*. 2024;269:114005. doi:10.1016/j.jpeds.2024.114005
12. Recica R, Kryeziu I, Thaci Q, et al. Protective effects of resveratrol against airway hyperreactivity, oxidative stress, and lung inflammation in a rat pup model of bronchopulmonary dysplasia. *Physiol Res*. 2024;73(2):239–251. doi:10.33549/physiolres.935239
13. Bao T, Liu X, Hu J, et al. Recruitment of PVT1 enhances YTHDC1-mediated m6A modification of IL-33 in hyperoxia-induced lung injury during bronchopulmonary dysplasia. *Inflammation*. 2024;47(2):469–482. doi:10.1007/s10753-023-01923-1

14. Hou W, Yu B, Li Y, et al. PC (16:0/14:0) ameliorates hyperoxia-induced bronchopulmonary dysplasia by upregulating claudin-1 and promoting alveolar type II cell repair. *Int J Biochem Cell Biol*. 2024;172:106587. doi:10.1016/j.biocel.2024.106587
15. Guo H, Huang RR, Qu SS, et al. FAM134B deletion exacerbates apoptosis and epithelial-to-mesenchymal transition in rat lungs exposed to hyperoxia. *iScience*. 2024;27(7):110385. doi:10.1016/j.isci.2024.110385
16. Chen P, Cheng Y, Hu J, et al. Recombinant CXCL17 treatment alleviates hyperoxia-induced lung apoptosis and inflammation in vivo and vitro by activating the AKT pathway: a possible therapeutic approach for bronchopulmonary dysplasia. *Mol Biotechnol*. 2024;66(9):2349–2361. doi:10.1007/s12033-023-00866-0
17. Wang MY, Yi MX, Mo XY, et al. Over-activation of iNKT cells aggravate lung injury in bronchopulmonary dysplasia mice. *Redox Biol*. 2024;77:103370. doi:10.1016/j.redox.2024.103370
18. Wang X, Yao F, Yang L, et al. Macrophage extracellular vesicle-packaged miR-23a-3p impairs maintenance and angiogenic capacity of human endothelial progenitor cells in neonatal hyperoxia-induced lung injury. *Stem Cell Res Ther*. 2024;15(1):295. doi:10.1186/s13287-024-03920-z
19. Xiong J, Ai Q, Bao L, et al. Dose-dependent effects of human umbilical cord-derived mesenchymal stem cell treatment in hyperoxia-induced lung injury of neonatal rats. *Front Pediatr*. 2023;11:1111829. doi:10.3389/fped.2023.1111829
20. Chou HC, Chang CH, Chen CH, et al. Consecutive daily administration of intratracheal surfactant and human umbilical cord-derived mesenchymal stem cells attenuates hyperoxia-induced lung injury in neonatal rats. *Stem Cell Res Ther*. 2021;12(1):258. doi:10.1186/s13287-021-02335-4
21. Cerro Marin MJD, Ormazabal IG, Gimeno-Navarro A, et al. Repeated intravenous doses of human umbilical cord-derived mesenchymal stromal cells for bronchopulmonary dysplasia: results of a Phase 1 clinical trial with 2-year follow-up. *Cytotherapy*. 2024;26(6):632–640. doi:10.1016/j.jcyt.2024.02.028
22. Pan W, Gu L, Yang H, et al. Repeat-dose toxicity study of human umbilical cord mesenchymal stem cells in cynomolgus monkeys by intravenous and subcutaneous injection. *Front Cell Dev Biol*. 2023;11:1273723. doi:10.3389/fcell.2023.1273723
23. Zhang S, Mulder C, Riddle S, et al. Mesenchymal stromal/stem cells and bronchopulmonary dysplasia. *Front Cell Dev Biol*. 2023;11:1247339. doi:10.3389/fcell.2023.1247339
24. Pote MS, Gacche RN. Exosomal signaling in cancer metastasis: molecular insights and therapeutic opportunities. *Arch Biochem Biophys*. 2024;764:110277. doi:10.1016/j.abb.2024.110277
25. Han M, Zhou X, Cheng H, et al. Chitosan and hyaluronic acid in colorectal cancer therapy: a review on EMT regulation, metastasis, and overcoming drug resistance. *Int J Biol Macromol*. 2024;289:138800. doi:10.1016/j.ijbiomac.2024.138800
26. Sun M, Li M, Hu M, et al. Fully bioactive nanodrugs: stem cell-derived exosomes engineered with biomacromolecules to treat CCl(4)- and extreme hepatectomy-induced acute liver failure. *ACS Nano*. 2024;18(50):33907–33921. doi:10.1021/acsnano.4c07408
27. Qiu AW, Wang NY, Yin WJ, et al. Retinal Muller cell-released exosomal MiR-92a-3p delivers interleukin-17A signal by targeting Notch-1 to promote diabetic retinopathy. *Invest Ophthalmol Vis Sci*. 2025;66(1):1. doi:10.1167/iovs.66.1.1
28. Zou D, Liao J, Xiao M, et al. Melatonin alleviates hyperoxia-induced lung injury through elevating MSC exosomal miR-18a-5p expression to repress PUM2 signaling. *FASEB J*. 2024;38(16):e70012. doi:10.1096/fj.202400374R
29. Chen C, Jin Y, Jin H, et al. Adipose mesenchymal stem cells-derived exosomes attenuated hyperoxia-induced lung injury in neonatal rats via inhibiting the NF-kappaB signaling pathway. *Pediatr Pulmonol*. 2024. doi:10.1002/ppul.27057
30. Ransom MA, Blatt AM, Pua HH, et al. The emerging role of extracellular vesicles in bronchopulmonary dysplasia. *Am J Physiol Lung Cell mol Physiol*. 2024;326(5):L517–L523. doi:10.1152/ajplung.00244.2023
31. Cheng T, Mao M, Liu Y, et al. The potential therapeutic effect of human umbilical cord mesenchymal stem cell-derived exosomes in bronchopulmonary dysplasia. *Life Sci*. 2024;357:123047. doi:10.1016/j.lfs.2024.123047
32. Li X, Huang L, Mao M, et al. HucMSCs-derived exosomes promote lung development in premature birth via Wnt5a/ROCK1 axis. *Stem Cell Rev Rep*. 2024. doi:10.1007/s12015-024-10824-1
33. Wang C, Jiang C, Yang Y, et al. Therapeutic potential of HUC-MSC-exos primed with IFN-gamma against LPS-induced acute lung injury. *Iran J Basic Med Sci*. 2024;27(3):375–382. doi:10.22038/IJBMS.2023.74372.16156
34. Pandey A, Immunomodulation MAK. Toxicity, and therapeutic potential of nanoparticles. *BioTech*. 2022;11(3). doi:10.3390/biotech11030042
35. Hu XM, Wang CC, Xiao Y, et al. Non-clinical safety evaluation of exosomes derived from human umbilical cord mesenchymal stem cells in cynomolgus monkeys. *Int J Nanomed*. 2024;19:4923–4939. doi:10.2147/IJN.S454438
36. Wan X, Fang Y, Du J, et al. GW4869 can inhibit epithelial-mesenchymal transition and extracellular HSP90alpha in gefitinib-sensitive NSCLC cells. *Onco Targets Ther*. 2023;16:913–922. doi:10.2147/OTT.S428707
37. Xu J, Liu G, Wang X, et al. hUC-MSCs: evaluation of acute and long-term routine toxicity testing in mice and rats. *Cytotechnology*. 2022;74(1):17–29. doi:10.1007/s10616-021-00502-2
38. Deng S, Li J, Li L, et al. Quercetin alleviates lipopolysaccharide-induced acute lung injury by inhibiting ferroptosis via the Sirt1/Nrf2/Gpx4 pathway. *Int J Mol Med*. 2023;52(6). doi:10.3892/ijmm.2023.5321
39. Wang L, Zhao W, Ning X, et al. Effect of X-ray irradiation combined with PD-1 inhibitor treatment on lung tissue injury in mice. *Int Immunopharmacol*. 2023;123:110775. doi:10.1016/j.intimp.2023.110775
40. Mecozzi L, Mambrini M, Ruscitti F, et al. In-vivo lung fibrosis staging in a bleomycin-mouse model: a new micro-CT guided densitometric approach. *Sci Rep*. 2020;10(1):18735. doi:10.1038/s41598-020-71293-3
41. Song S, Fu Z, Guan R, et al. Intracellular hydroxyproline imprinting following resolution of bleomycin-induced pulmonary fibrosis. *Eur Respir J*. 2022;59(5). doi:10.1183/13993003.00864-2021
42. Wu J, Huang QM, Liu Y, et al. Long-term hypoxic hUCMSCs-derived extracellular vesicles alleviates allergic rhinitis through triggering immunotolerance of their VEGF-mediated inhibition of dendritic cells maturation. *Int Immunopharmacol*. 2023;124(Pt B):110875. doi:10.1016/j.intimp.2023.110875
43. Bisaccia P, Magarotto F, D'Agostino S, et al. Extracellular vesicles from mesenchymal umbilical cord cells exert protection against oxidative stress and fibrosis in a rat model of bronchopulmonary dysplasia. *Stem Cells Transl Med*. 2024;13(1):43–59. doi:10.1093/stcltm/szad070
44. El azzouzi M, El Ahanidi H, Hassan I, et al. Comprehensive behavioural assessment of TERT in bladder cancer. *Urol Oncol*. 2024. doi:10.1016/j.urolonc.2024.06.024

45. Zhang Y, He X, Ge Z, et al. Investigating the differential therapeutic efficacy and mechanisms of human umbilical cord mesenchymal stem cells at various passages in osteoarthritis treatment. *Tissue Cell*. 2024;90:102499. doi:10.1016/j.tice.2024.102499
46. Hao X, Zhu H, Qin C, et al. Study on preclinical safety and toxic mechanism of human umbilical cord mesenchymal stem cells in F344RG rats. *Stem Cell Rev Rep*. 2024. doi:10.1007/s12015-024-10780-w
47. Sachpekidis C, Stein-Thoeringer CK, Kopp-Schneider A, et al. Can physiologic colonic [(18)F]FDG uptake in PET/CT imaging predict response to immunotherapy in metastatic melanoma? *Eur J Nucl Med Mol Imaging*. 2023;50(12):3709–3722. doi:10.1007/s00259-023-06327-9
48. Chin SP, Saffery NS, Then KY, et al. Preclinical assessments of safety and tumorigenicity of very high doses of allogeneic human umbilical cord mesenchymal stem cells. *Ex Vivo Cell Dev Biol Anim*. 2024;60(3):307–319. doi:10.1007/s11626-024-00852-z
49. Zhao Q, Zhang L, Wei Y, et al. Systematic comparison of hUC-MSCs at various passages reveals the variations of signatures and therapeutic effect on acute graft-versus-host disease. *Stem Cell Res Ther*. 2019;10(1):354. doi:10.1186/s13287-019-1478-4
50. Xie Y, Liu S, Wang L, et al. Individual heterogeneity screened umbilical cord-derived mesenchymal stromal cells with high Treg promotion demonstrate improved recovery of mouse liver fibrosis. *Stem Cell Res Ther*. 2021;12(1):359. doi:10.1186/s13287-021-02430-6
51. Koide T, Mandai S, Kitaoka R, et al. Circulating extracellular vesicle-propagated microRNA signature as a vascular calcification factor in chronic kidney disease. *Circ Res*. 2023;132(4):415–431. doi:10.1161/CIRCRESAHA.122.321939
52. Zou W, Lai M, Jiang Y, et al. Exosome release delays senescence by disposing of obsolete biomolecules. *Adv Sci*. 2023;10(8):e2204826. doi:10.1002/advs.202204826
53. Liu M, Ng M, Phu T, et al. Polarized macrophages regulate fibro/adipogenic progenitor (FAP) adipogenesis through exosomes. *Stem Cell Res Ther*. 2023;14(1):321. doi:10.1186/s13287-023-03555-6
54. Zhou X, Zhao S, Li W, et al. Tubular cell-derived exosomal miR-150-5p contributes to renal fibrosis following unilateral ischemia-reperfusion injury by activating fibroblast ex vivo and in vivo. *Int J Biol Sci*. 2021;17(14):4021–4033. doi:10.7150/ijbs.62478
55. Ao M, Ma H, Guo M, et al. Research hotspots and emerging trends in mesenchymal stem/stromal cells in bronchopulmonary dysplasia. *Hum Cell*. 2024;37(2):381–393. doi:10.1007/s13577-023-01018-x
56. Nguyen LT, Trieu TTH, Bui HTH, et al. Allogeneic administration of human umbilical cord-derived mesenchymal stem/stromal cells for bronchopulmonary dysplasia: preliminary outcomes in four Vietnamese infants. *J Transl Med*. 2020;18(1):398. doi:10.1186/s12967-020-02568-6
57. Li X, Huang Q, Zhang X, et al. Reproductive and developmental toxicity assessment of human umbilical cord mesenchymal stem cells in rats. *Front Cell Dev Biol*. 2022;10:883996. doi:10.3389/fcell.2022.883996
58. Cheng WD, Bin L, Lin ZX, et al. Human umbilical cord mesenchymal stem cells toxicity and allergy effects: in vivo assessment. *PLoS One*. 2024;19(10):e0309429. doi:10.1371/journal.pone.0309429
59. Wu X, Xia Y, Zhou O, et al. Allogeneic human umbilical cord-derived mesenchymal stem cells for severe bronchopulmonary dysplasia in children: study protocol for a randomized controlled trial (MSC-BPD trial). *Trials*. 2020;21(1):125. doi:10.1186/s13063-019-3935-x
60. Wang L, Xiao J, Zhang B, et al. Epigenetic modifications in the development of bronchopulmonary dysplasia: a review. *Pediatr Res*. 2024. doi:10.1038/s41390-024-03167-7
61. Sun Y, Chen C, Liu Y, et al. Adipose stem cells derived exosomes alleviate bronchopulmonary dysplasia and regulate autophagy in neonatal rats. *Curr Stem Cell Res Ther*. 2024;19(6):919–932. doi:10.2174/011574888X260261230928094309
62. Albertine KH, Rebentisch A, Dawson E, et al. Mesenchymal stromal cell extracellular vesicles improve lung development in mechanically ventilated preterm lambs. *Am J Physiol Lung Cell Mol Physiol*. 2024;326(6):L770–L785. doi:10.1152/ajplung.00349.2023
63. Li Y, Yu B, Li H, et al. Human milk exosome-derived circDNAJB6 improves bronchopulmonary dysplasia model by promoting DNAJB6 gene transcription. *J Bioenerg Biomembr*. 2024;56(2):171–180. doi:10.1007/s10863-024-10002-5
64. Saneh H, Wanczyk H, Walker J, et al. Effectiveness of extracellular vesicles derived from hiPSCs in repairing hyperoxia-induced injury in a fetal murine lung explant model. *Stem Cell Res Ther*. 2024;15(1):80. doi:10.1186/s13287-024-03687-3
65. Zhong XQ, Hao TF, Zhu QJ, et al. Umbilical cord blood exosomes from very preterm infants with bronchopulmonary dysplasia aggravate lung injury in mice. *Sci Rep*. 2023;13(1):8648. doi:10.1038/s41598-023-35620-8
66. Costa-Ferro ZSM, Rocha GV, da Silva KN, et al. GMP-compliant extracellular vesicles derived from umbilical cord mesenchymal stromal cells: manufacturing and pre-clinical evaluation in ARDS treatment. *Cytotherapy*. 2024;26(9):1013–1025. doi:10.1016/j.jcyt.2024.04.074
67. Lesage F, Thebaud B. Mesenchymal stromal cell-derived extracellular vesicles for neonatal lung disease: tiny particles, major promise, rigorous requirements for clinical translation. *Cells*. 2022;11(7). doi:10.3390/cells11071176
68. Collaco JM, Eldredge LC, McGrath-Morrow SA. Long-term pulmonary outcomes in BPD throughout the life-course. *J Perinatol*. 2024. doi:10.1038/s41372-024-01957-9
69. Nardiello C, Mizikova I, Morty RE. Looking ahead: where to next for animal models of bronchopulmonary dysplasia? *Cell Tissue Res*. 2017;367(3):457–468. doi:10.1007/s00441-016-2534-3
70. Loering S, Cameron GJM, Starkey MR, et al. Lung development and emerging roles for type 2 immunity. *J Pathol*. 2019;247(5):686–696. doi:10.1002/path.5211
71. Zanini F, Che X, Suresh NE, et al. Hyperoxia prevents the dynamic neonatal increases in lung mesenchymal cell diversity. *Sci Rep*. 2024;14(1):2033. doi:10.1038/s41598-023-50717-w
72. Yu B, Jia S, Chen Y, et al. CXCL4 deficiency limits M4 macrophage infiltration and attenuates hyperoxia-induced lung injury. *Mol Med*. 2024;30(1):253. doi:10.1186/s10020-024-01043-y
73. Hurskainen M, Mizikova I, Cook DP, et al. Single cell transcriptomic analysis of murine lung development on hyperoxia-induced damage. *Nat Commun*. 2021;12(1):1565. doi:10.1038/s41467-021-21865-2
74. Fusco C, De Rosa G, Spatocco I, et al. Extracellular vesicles as human therapeutics: a scoping review of the literature. *J Extracell Vesicles*. 2024;13(5):e12433. doi:10.1002/jev2.12433
75. Sengupta V, Sengupta S, Lazo A, et al. Exosomes derived from bone marrow mesenchymal stem cells as treatment for severe COVID-19. *Stem Cells Dev*. 2020;29(12):747–754. doi:10.1089/scd.2020.0080
76. Lightner AL, Sengupta V, Qian S, et al. Bone marrow mesenchymal stem cell-derived extracellular vesicle infusion for the treatment of respiratory failure from COVID-19: a randomized, placebo-controlled dosing clinical trial. *Chest*. 2023;164(6):1444–1453. doi:10.1016/j.chest.2023.06.024

77. Zhu YG, Shi MM, Monsel A, et al. Nebulized exosomes derived from allogenic adipose tissue mesenchymal stromal cells in patients with severe COVID-19: a pilot study. *Stem Cell Res Ther*. 2022;13(1):220. doi:10.1186/s13287-022-02900-5
78. Mitrani MI, Bellio MA, Meglin A, et al. Treatment of a COVID-19 long hauler with an amniotic fluid-derived extracellular vesicle biologic. *Respir Med Case Rep*. 2021;34:101502. doi:10.1016/j.rmcr.2021.101502
79. Mitrani MI, Bellio MA, Sagel A, et al. Case report: administration of amniotic fluid-derived nanoparticles in three severely ill COVID-19 patients. *Front Med*. 2021;8:583842. doi:10.3389/fmed.2021.583842
80. Bellio MA, Bennett C, Arango A, et al. Proof-of-concept trial of an amniotic fluid-derived extracellular vesicle biologic for treating high risk patients with mild-to-moderate acute COVID-19 infection. *Biomater Biosyst*. 2021;4:100031. doi:10.1016/j.bbiosy.2021.100031
81. Zarrabi M, Shahrbaf MA, Nouri M, et al. Allogenic mesenchymal stromal cells and their extracellular vesicles in COVID-19 induced ARDS: a randomized controlled trial. *Stem Cell Res Ther*. 2023;14(1):169. doi:10.1186/s13287-023-03402-8
82. Shi MM, Yang QY, Monsel A, et al. Preclinical efficacy and clinical safety of clinical-grade nebulized allogenic adipose mesenchymal stromal cells-derived extracellular vesicles. *J Extracell Vesicles*. 2021;10(10):e12134. doi:10.1002/jev2.12134
83. Goryunov K, Ivanov M, Kulikov A, et al. A review of the use of extracellular vesicles in the treatment of neonatal diseases: current state and problems with translation to the clinic. *Int J Mol Sci*. 2024;25(5). doi:10.3390/ijms25052879
84. Abele AN, Taglauer ES, Almeda M, et al. Antenatal mesenchymal stromal cell extracellular vesicle treatment preserves lung development in a model of bronchopulmonary dysplasia due to chorioamnionitis. *Am J Physiol Lung Cell Mol Physiol*. 2022;322(2):L179–L190. doi:10.1152/ajplung.00329.2021
85. Bellio MA, Young KC, Milberg J, et al. Amniotic fluid-derived extracellular vesicles: characterization and therapeutic efficacy in an experimental model of bronchopulmonary dysplasia. *Cytotherapy*. 2021;23(12):1097–1107. doi:10.1016/j.jcyt.2021.07.011
86. Wang J, Zhang A, Huang F, et al. MSC-EXO and tempol ameliorate bronchopulmonary dysplasia in newborn rats by activating HIF-1alpha. *Pediatr Pulmonol*. 2023;58(5):1367–1379. doi:10.1002/ppul.26317
87. Pugh CP, Ali S, Agarwal A, et al. Dynamic computed tomography for evaluation of tracheobronchomalacia in premature infants with bronchopulmonary dysplasia. *Pediatr Pulmonol*. 2023;58(11):3255–3263. doi:10.1002/ppul.26652
88. Fontijn S, Balink SJA, Bonte M, et al. Chest computed tomography in severe bronchopulmonary dysplasia: comparing quantitative scoring methods. *Eur J Radiol*. 2023;169:111168. doi:10.1016/j.ejrad.2023.111168
89. Smith EF, Hemy NR, Hall GL, et al. Risk factors for poorer respiratory outcomes in adolescents and young adults born preterm. *Thorax*. 2023;78(12):1223–1232. doi:10.1136/thorax-2022-219634
90. Shin JE, Lee SM, Lee MJ, et al. Oligohydramnios affects pulmonary functional/structural abnormalities in school-aged children with bronchopulmonary dysplasia. *Clin Exp Pediatr*. 2024;67(5):257–266. doi:10.3345/cep.2023.01053
91. Sato H, Kato A, Adachi H, et al. High oxygen exposure's impact on newborn mice: temporal changes observed via micro-computed tomography. *Exp Lung Res*. 2024;50(1):127–135. doi:10.1080/01902148.2024.2375099
92. Ivanciuc T, Patrikeev I, Qu Y, et al. Micro-CT features of lung consolidation, collagen deposition and inflammation in experimental RSV infection are aggravated in the absence of Nrf2. *Viruses*. 2023;15(5). doi:10.3390/v15051191
93. McGinn EA, Bye E, Gonzalez T, et al. Antenatal endotoxin induces dysanapsis in experimental bronchopulmonary dysplasia. *Am J Respir Cell Mol Biol*. 2024;70(4):283–294. doi:10.1165/rcmb.2023-0157OC
94. Sucre JMS, Vickers KC, Benjamin JT, et al. Hyperoxia injury in the developing lung is mediated by mesenchymal expression of Wnt5A. *Am J Respir Crit Care Med*. 2020;201(10):1249–1262. doi:10.1164/rccm.201908-1513OC
95. Hirani D, Alvira CM, Danopoulos S, et al. Macrophage-derived IL-6 trans-signalling as a novel target in the pathogenesis of bronchopulmonary dysplasia. *Eur Respir J*. 2022;59(2). doi:10.1183/13993003.02248-2020
96. Gong SC, Yoon Y, Jung PY, et al. Antifibrotic TSG-6 expression is synergistically increased in both cells during coculture of mesenchymal stem cells and macrophages via the JAK/STAT signaling pathway. *Int J Mol Sci*. 2022;23(21). doi:10.3390/ijms232113122
97. Liu J, Chen T, Lei P, et al. Exosomes released by bone marrow mesenchymal stem cells attenuate lung injury induced by intestinal ischemia reperfusion via the TLR4/NF-kappaB pathway. *Int J Med Sci*. 2019;16(9):1238–1244. doi:10.7150/ijms.35369
98. Zhong XQ, Wang D, Chen S, et al. Umbilical cord blood-derived exosomes from healthy term pregnancies protect against hyperoxia-induced lung injury in mice. *Clin Transl Sci*. 2023;16(6):966–977. doi:10.1111/cts.13502
99. Durlak W, Thebaud B. The vascular phenotype of BPD: new basic science insights-new precision medicine approaches. *Pediatr Res*. 2024;96(5):1162–1171. doi:10.1038/s41390-022-02428-7
100. Tian H, Chen A, Gao P, et al. Human umbilical cord mesenchymal stem cell-derived exosomes induce macrophage M2 polarization by antagonizing LPS-mediated stimulation of the NF-kappaB and STAT3 pathways. *Comb Chem High Throughput Screen*. 2024. doi:10.2174/0113862073314685240514050119
101. Li L, Zhang X, Chen Y. Human umbilical cord mesenchymal stem cell exosome-derived miR-335-5p alleviated lipopolysaccharide-induced acute lung injury by regulating the m6A level of ITGbeta4 gene. *Curr Med Chem*. 2024;31(33):5448–5467. doi:10.2174/0109298673273833231220062213
102. Deng H, Zhu L, Zhang Y, et al. Differential lung protective capacity of exosomes derived from human adipose tissue, bone marrow, and umbilical cord mesenchymal stem cells in sepsis-induced acute lung injury. *Oxid Med Cell Longev*. 2022;2022:7837837. doi:10.1155/2022/7837837
103. Wang X, Cui L, Wang Y, et al. Mechanistic investigation of wogonin in delaying the progression of endothelial mesenchymal transition by targeting the TGF-β1 pathway in pulmonary hypertension. *Eur J Pharmacol*. 2024;978:176786. doi:10.1016/j.ejphar.2024.176786
104. Huang C, Liang C, Tong J, et al. Soluble E-cadherin participates in BLM-induced pulmonary fibrosis by promoting EMT and lung fibroblast migration. *Environ Toxicol*. 2024;39(1):435–443. doi:10.1002/tox.23986
105. Gupta V, Singh S, Singh TG. Pervasive expostulation of p53 gene promoting the precipitation of neurogenic convulsions: a journey in therapeutic advancements. *Eur J Pharmacol*. 2024;983:176990. doi:10.1016/j.ejphar.2024.176990
106. Ikeda T, Kawabori M, Zheng Y, et al. Intranasal administration of mesenchymal stem cell-derived exosome alleviates hypoxic-ischemic brain injury. *Pharmaceutics*. 2024;16(4). doi:10.3390/pharmaceutics16040446
107. Gu Z, Yin Z, Song P, et al. Safety and biodistribution of exosomes derived from human induced pluripotent stem cells. *Front Bioeng Biotechnol*. 2022;10:949724. doi:10.3389/fbioe.2022.949724

108. Dinh PC, Paudel D, Brochu H, et al. Inhalation of lung spheroid cell secretome and exosomes promotes lung repair in pulmonary fibrosis. *Nat Commun*. 2020;11(1):1064. doi:10.1038/s41467-020-14344-7
109. Ren J, Liu Y, Yao Y, et al. Intranasal delivery of MSC-derived exosomes attenuates allergic asthma via expanding IL-10 producing lung interstitial macrophages in mice. *Int Immunopharmacol*. 2021;91:107288. doi:10.1016/j.intimp.2020.107288
110. Gotoh S, Kawabori M, Fujimura M. Intranasal administration of stem cell-derived exosomes for central nervous system diseases. *Neural Regen Res*. 2024;19(6):1249–1255. doi:10.4103/1673-5374.385875
111. Pomatto MAC, Gai CR, Negro F, et al. Plant-derived extracellular vesicles as a delivery platform for RNA-based vaccine: feasibility study of an oral and intranasal SARS-CoV-2 vaccine. *Pharmaceutics*. 2023;15(3):974.
112. Chen Y, Shi Y, Tao Z. Fluorescence tracking of small extracellular vesicles in vivo. *Pharmaceutics*. 2023;15(9). doi:10.3390/pharmaceutics15092297
113. Xia L, Zhang C, Lv N, et al. AdMSC-derived exosomes alleviate acute lung injury via transferring mitochondrial component to improve homeostasis of alveolar macrophages. *Theranostics*. 2022;12(6):2928–2947. doi:10.7150/thno.69533
114. Valiukevicius P, Maciulaitis J, Pangonyte D, et al. Human placental mesenchymal stem cells and derived extracellular vesicles ameliorate lung injury in acute respiratory distress syndrome murine model. *Cells*. 2023;12(23). doi:10.3390/cells12232729
115. Hirani DV, Thielen F, Mansouri S, et al. CXCL10 deficiency limits macrophage infiltration, preserves lung matrix, and enables lung growth in bronchopulmonary dysplasia. *Inflamm Regen*. 2023;43(1):52. doi:10.1186/s41232-023-00301-6
116. Ivanovski N, Wang H, Tran H, et al. L-citrulline attenuates lipopolysaccharide-induced inflammatory lung injury in neonatal rats. *Pediatr Res*. 2023;94(5):1684–1695. doi:10.1038/s41390-023-02684-1
117. Yu H, Li D, Zhao X, et al. Fetal origin of bronchopulmonary dysplasia: contribution of intrauterine inflammation. *Mol Med*. 2024;30(1):135. doi:10.1186/s10020-024-00909-5
118. Calthorpe RJ, Poulter C, Smyth AR, et al. Complex roles of TGF-beta signaling pathways in lung development and bronchopulmonary dysplasia. *Am J Physiol Lung Cell Mol Physiol*. 2023;324(3):L285–L296. doi:10.1152/ajplung.00106.2021
119. Goodwin AT, John AE, Joseph C, et al. Stretch regulates alveologenesis and homeostasis via mesenchymal Galphaq/11-mediated TGFbeta2 activation. *Development*. 2023;150(9). doi:10.1242/dev.201046
120. Deng S, Zhang H, Han W, et al. Transforming growth factor-beta-neutralizing antibodies improve alveolarization in the oxygen-exposed newborn mouse lung. *J Interferon Cytokine Res*. 2019;39(2):106–116. doi:10.1089/jir.2018.0080
121. Ye Z, Hu Y. TGF-β1: gentlemanly orchestrator in idiopathic pulmonary fibrosis (Review). *Int J Mol Med*. 2021;48(1). doi:10.3892/ijmm.2021.4965
122. Roeder F, Ropke T, Steinmetz LK, et al. Exploring alveolar recruitability using positive end-expiratory pressure in mice overexpressing TGF-β1: a structure-function analysis. *Sci Rep*. 2024;14(1):8080. doi:10.1038/s41598-024-58213-5
123. Beike L, Wrede C, Hegermann J, et al. Surfactant dysfunction and alveolar collapse are linked with fibrotic septal wall remodeling in the TGF-β1-induced mouse model of pulmonary fibrosis. *Lab Invest*. 2019;99(6):830–852. doi:10.1038/s41374-019-0189-x
124. Huang Y, Wu Q, Tam PKH. Immunomodulatory mechanisms of mesenchymal stem cells and their potential clinical applications. *Int J Mol Sci*. 2022;23(17). doi:10.3390/ijms231710023
125. Wang Y, Liu C, Wang N, et al. hAMSCs regulate EMT in the progression of experimental pulmonary fibrosis through delivering miR-181a-5p targeting TGFBR1. *Stem Cell Res Ther*. 2025;16(1):2. doi:10.1186/s13287-024-04095-3
126. Obendorf J, Fabian C, Thome UH, et al. Paracrine stimulation of perinatal lung functional and structural maturation by mesenchymal stem cells. *Stem Cell Res Ther*. 2020;11(1):525. doi:10.1186/s13287-020-02028-4
127. Eldredge LC, Creasy RS, Presnell S, et al. Infants with evolving bronchopulmonary dysplasia demonstrate monocyte-specific expression of IL-1 in tracheal aspirates. *Am J Physiol Lung Cell Mol Physiol*. 2019;317(1):L49–L56. doi:10.1152/ajplung.00060.2019
128. Golubinskaya V, Nilsson H, Rydbeck H, et al. Cytokine and growth factor correlation networks associated with morbidities in extremely preterm infants. *BMC Pediatr*. 2024;24(1):723. doi:10.1186/s12887-024-05203-1
129. Zheng X, Tan Z, Zhu D, et al. Eclipta prostrata improves alveolar development of bronchopulmonary dysplasia via suppressing the NLRP3 inflammasome in a DLD-dependent manner. *Pediatr Pulmonol*. 2024;59(12):3371–3382. doi:10.1002/ppul.27209
130. Young K, Benny M, Schmidt A, et al. Unveiling the emerging role of extracellular vesicle-inflammasomes in hyperoxia-induced neonatal lung and brain injury. *Cells*. 2024;13(24). doi:10.3390/cells13242094
131. Liao J, Kapadia VS, Brown LS, et al. The NLRP3 inflammasome is critically involved in the development of bronchopulmonary dysplasia. *Nat Commun*. 2015;6:8977. doi:10.1038/ncomms9977
132. Li J, Sun S, Zhu D, et al. Inhalable stem cell exosomes promote heart repair after myocardial infarction. *Circulation*. 2024;150(9):710–723. doi:10.1161/CIRCULATIONAHA.123.065005